

## Full length article

## Multi-scale characterization of austenite reversion and martensite recovery in a cold-rolled medium-Mn steel

J.T. Benzing<sup>a,\*</sup>, A. Kwiatkowski da Silva<sup>b</sup>, L. Morsdorf<sup>b</sup>, J. Bentley<sup>c</sup>, D. Ponge<sup>b</sup>, A. Dutta<sup>b</sup>, J. Han<sup>d</sup>, J.R. McBride<sup>e</sup>, B. Van Leer<sup>f</sup>, B. Gault<sup>b</sup>, D. Raabe<sup>b</sup>, J.E. Wittig<sup>a</sup>

<sup>a</sup> Interdisciplinary Materials Science, Vanderbilt University, Nashville, TN, 37235-1683, USA

<sup>b</sup> Max-Planck-Institut für Eisenforschung, Max-Planck-Str. 1, 40237, Düsseldorf, Germany

<sup>c</sup> Microscopy and Microanalytical Sciences, PO Box 7103, Oak Ridge, TN 37831, 7103, USA

<sup>d</sup> Materials Science and Engineering, Chungnam National University, Daejeon, 34134, Republic of Korea

<sup>e</sup> Vanderbilt Institute of Nanoscale Science and Engineering, Vanderbilt University, Nashville, TN 37232, USA

<sup>f</sup> Thermo Fisher Scientific, 5350 NE Dawson Creek Drive, Hillsboro, OR, 97124, USA

## ARTICLE INFO

## Article history:

Received 6 September 2018

Received in revised form

30 November 2018

Accepted 3 January 2019

Available online 7 January 2019

## Keywords:

Austenite reversion

Martensite recovery

Medium-Mn steel

FIB tomography

3D EBSD

STEM EDS

Atom probe tomography

Thermo-Calc<sup>®</sup>

DICTRA

## ABSTRACT

A medium-Mn steel (Fe-12Mn-3Al-0.05C wt%) was designed using Thermo-Calc<sup>®</sup> simulations to balance the fraction and stacking fault energy of reverted austenite. Intercritical annealing for 0.5, 8 and 48 h was carried out at 585 °C to investigate the microstructural evolution. X-ray diffraction (XRD), electron backscatter diffraction (EBSD), 3-dimensional EBSD, energy-dispersive spectroscopy via scanning-transmission electron microscopy (STEM-EDS) and atom probe tomography (APT) enable characterization of phase fraction, grain area, grain morphology and alloy partitioning. An increase in annealing time from 0.5 h to 48 h increases the amount of ultrafine-grained (UFG) reverted austenite from 3 to 40 vol %. EBSD and TEM reveal multiple morphologies of UFG austenite (equiaxed, rod-like and plate-like). In addition, most of the remaining microstructure consists of recovered  $\alpha'$ -martensite that resembles the cold-rolled state, as well as a relatively small fraction of UFG ferrite (i.e., only a small amount of martensite recrystallization occurs). Multi-scale characterization results show that the location within the cold-rolled microstructure has a strong influence on boundary mobility and grain morphology during austenite reversion. Results from APT reveal Mn-decoration of dislocation networks and low-angle lath boundaries in the recovered  $\alpha'$ -martensite, but an absence of Mn-decoration of defects in the vicinity of austenite grains, thereby promoting recovery. STEM-EDS and APT reveal Mn depletion zones in the ferrite/recovered  $\alpha'$ -martensite near austenite boundaries, whereas gradients of C and Mn co-partitioning are visible within some of the austenite grains after annealing for 0.5 h. Relatively flat C-enriched austenite boundaries are present even after 8 h of annealing and indicate certain boundaries possess low mobility. At later stages the growth of austenite followed the local equilibrium (LE) model such that the driving force between two equilibrium phases moves the mobile interface, as confirmed by DICTRA simulations (a Thermo-Calc<sup>®</sup> diffusion module). The sequence of austenite reversion is: (i) formation of Mn- and C-enriched face-centered-cubic nuclei from decorated dislocations and/or particles; (ii) co-partitioning of Mn and C and (iii) growth of austenite controlled by the LE mode.

© 2019 Acta Materialia Inc. Published by Elsevier Ltd. All rights reserved.

## 1. Introduction

Medium-Mn steels are considered third-generation advanced high-strength steels (AHSS) and aim to balance the low cost of first-

generation AHSS with the outstanding mechanical properties of second-generation AHSS, especially for automotive applications [1–5]. An optimally balanced third-generation AHSS possesses a total alloying content below 17 wt% and a multi-phase microstructure consisting of  $\alpha'$ -martensite, ferrite and austenite. Medium-Mn steels with Mn contents between 3 and 15 wt% generally exhibit a deformed  $\alpha'$ -martensitic microstructure after cold rolling [6,7]. Intercritical annealing produces ultrafine-grained (UFG) austenite and ferrite at temperatures in the  $\alpha+\gamma$  phase field

\* Corresponding author. Currently at the National Institute of Standards and Technology, Boulder, CO, USA.

E-mail address: [jake.benzing@nist.gov](mailto:jake.benzing@nist.gov) (J.T. Benzing).

that also coincide with a temperature regime for  $\alpha'$ -martensite recrystallization [8]. This annealing stage is a critical processing step in medium-Mn steel production as the annealing temperature and time strongly affect the fractions and sizes of the reverted austenite and recrystallized ferrite [9]. After nucleation, the partitioning of Mn and C during intercritical annealing controls the amount, size, composition and stacking fault energy (SFE) of the reverted austenite. In most cases for medium-Mn steel production, an increase in intercritical annealing temperature decreases the Mn content in austenite and decreases the SFE of the austenite [10,11]. The SFE controls transformation- and twinning-induced plasticity (TRIP and TWIP) effects in the austenite during deformation which increase the strain-hardening rate of the material [9,12–16].

Given the same intercritical annealing time and temperature, both bulk composition and the amount of cold rolling allow for tuning of fractions and morphologies of the constituent phases, which in turn greatly influence mechanical properties [6]. Other researchers of medium-Mn steels, TRIP steels and TWIP steels have observed static and dynamic strain-aging effects, respectively termed Lüders bands and Portevin-Le Chatelier (PLC) bands, which can lead to plastic instabilities during deformation [17–19]. Recent work on bulk compositions similar to the current work [20,21] indicates no evidence of Lüders and PLC bands. The presence of discontinuous yielding is usually attributed to the complete recrystallization and equiaxed morphology of the microstructure, the grain size of the UFG ferrite and the relatively low yield strength of ferrite (compared to austenite) [8,11,22–26]. Non-equiaxed microstructures can be advantageous in fatigue-critical applications. In fact, a recent study [27] on a medium-Mn steel with a bulk composition and microstructure similar to those in the current work showed superior low-cycle fatigue-life limits due to a nano-laminate multi-phase meta-stable microstructure that provided tortuous paths to limit crack propagation [28]. In terms of tensile properties, the UFG austenite and ferrite are likely to produce high yield strengths from the Hall-Petch relationship [22]. Further, recent techniques also utilize additions of V and C in medium-Mn steels to produce extremely hard carbides and thus higher strength materials [29,30]. Characterizing partitioning and final compositions in this work will be important in understanding the mechanical behavior of the constituent phases in this multi-phase steel [31,32] to better inform constitutive models [33] for predicting mechanical properties in future work. By providing a more complete understanding of the microstructural evolution, future work in alloy design can then exploit competing mechanisms to manipulate the microstructure and thus mechanical properties.

In terms of compositional evolution of the microstructure, Chen et al. [34] measured Mn and C concentrations in austenite that were greater at lower annealing temperatures in an Fe-5.1Mn-1.4Ni-0.2Si-0.035C wt% steel (10.4Mn-0.12C wt% in austenite at 600 °C vs 7.7Mn-0.07C wt% in austenite at 650 °C). Work by Lee et al. [9] on an Fe-6Mn-0.3C wt% steel demonstrated that an increase in intercritical annealing temperature increased the equilibrium austenite volume fraction, up until a specific temperature ( $T_{\gamma\text{-max}}$ ), above which the austenite volume fraction measured at room temperature (RT) decreased. The decrease in RT austenite fraction after intercritical annealing and quenching with temperatures above  $T_{\gamma\text{-max}}$  is due to the formation of fresh athermal  $\alpha'$ -martensite during cooling.  $T_{\gamma\text{-max}}$  varies strongly with carbon content and moderately with parent grain size [9,35]. In addition, the volume fraction and grain size of reverted austenite, which inherently influences mechanical properties, depends on annealing time and temperature [6,36]. For an Fe-6Mn-0.3C wt% steel, Lee et al. [9] observed an increase in austenite fraction from 10 to 25% upon increasing annealing from 1 h to 24 h at 600 °C. Specific to nucleation, recent

work on an Fe-7Mn-0.1C-0.5Si (wt%) steel by Kwiatkowski da Silva et al. showed that both austenite and carbide nucleation at 450 °C depends on the co-segregation of C and Mn to dislocations and grain boundaries [37]. Consequently, when the carbon content is high enough, the nucleation of austenite may be delayed due to the competition with the formation of carbides.

In this work, changes in annealing time allow for the investigation of the compositional and morphological evolution of the multi-phase microstructure. One focus of the present work was to design a low-carbon medium-Mn steel (informed by Thermo-Calc<sup>®</sup> and DICTRA simulations) with a multi-phase microstructure containing UFG austenite with an austenite composition that corresponds to a predicted RT SFE of approximately 20 mJ/m<sup>2</sup>. This RT SFE is desirable since recent studies [3,38–41] on coarse-grained high-Mn steels with a similar SFE show evidence of both mechanical twinning and  $\epsilon$ -martensite formation in the same grain. The characterization of a multi-phase medium-Mn steel is particularly challenging as the austenite is ultrafine in size (<500 nm), plus most of the microstructure is recovered or recrystallized  $\alpha'$ -martensite regions, which are ferromagnetic and thus increase the difficulty of transmission electron microscopy (TEM) analysis. Energy-dispersive spectroscopy via scanning-transmission electron microscopy (STEM-EDS) and atom probe tomography (APT) quantify the compositions of the ultrafine-grained (UFG) austenite after intercritical annealing and provide an indicator of RT SFE of the austenite. The multi-scale characterization approach in this work identifies key compositional features of austenite reversion, martensite recovery and martensite recrystallization, such as nucleation sites, co-partitioning, Mn-decorated defects, Mn depletion zones, and C enrichment on flat interfaces and/or near triple-junctions. Electron backscatter diffraction (EBSD) reconstructions in both 2 and 3 dimensions highlight the multiple morphologies of austenite (equiaxed, rod-like and plate-like) and their origin. EBSD, TEM and APT reveal the influence of location (near equiaxed UFG ferrite, prior austenite boundaries and lath martensite boundaries) on reverted austenite morphology and boundary mobility.

## 2. Experimental methods

### 2.1. Material

To create the bulk material, an ingot of Fe-12Mn-3Al-0.05C (wt %) was hot-rolled between 1100 °C and 900 °C to 3.4 mm thickness, homogenized in an Ar atmosphere at 1100 °C for 2 h and water-quenched to RT, which is below the Ms temperature. After quenching, the sheet was cold-rolled to 1.7 mm (a 50% reduction in thickness) to produce a deformed martensitic microstructure. Micro-hardness (Vickers scale) was measured using a 2 kg load and an average of 7 indents. Dilatometer measurements were carried out under vacuum (specimen dimensions of 9 mm × 4 mm × 1.7 mm) using a Bähr Dil805 model, equipped with induction heating at 32 kHz. A supply of He was used for the cooling medium. To determine Ac1 and Ac3 temperatures, dilatometer specimens were heated to 950 °C at 10 °C/s, held for 60 s and cooled at 10 °C/s. To study the effect of intercritical annealing time on the microstructure, the cold-rolled sheets of medium-Mn steel were annealed at 585 °C for 0.5 h, 8 h and 48 h, using a heating rate of 100 °C/s and a cooling rate of 100 °C/s. Since the local microstructure may be strongly influenced by Mn segregation, EDS mapping was performed at low magnification in the SEM on a bulk cold-rolled specimen annealed for 8 h at 585 °C, but no Mn-banding or other large-scale segregation was observed. Such phenomena have been observed in hot-rolled medium-Mn steels [30].

## 2.2. Sample preparation and microstructural characterization

### 2.2.1. EBSD and XRD

To prepare samples for characterization with electron backscatter diffraction (EBSD), sections of the intercritically annealed material were mounted in conductive Bakelite, noting the rolling direction, ground with SiC paper and auto-polished with diamond paste and a final step using 50 nm silica. EBSD measurements were acquired using a JEOL JSM-6500F FESEM with the following SEM and scan parameters: 15 keV accelerating voltage, 12 nA probe current, 18 mm working distance and a 30 nm step size. Data cleanup involved a grain confidence-index standardization. 3-dimensional (3D) EBSD measurements were completed using a Thermo Scientific Helios G4 plasma focused ion beam (PFIB) operated at 20 keV and equipped with EBS3™ software. A fiducial mark was placed on the Cu post near the section of material to locate the same region of interest between EBSD scans. The 30 keV FIB was operated at 6.7 nA and sliced away material every 10 nm at a 4 mm working distance (including alternating slices with 5° of rocking side-to-side). EBSD maps were recorded using a 50 nm step size after every 5 slices (after 50 nm of material was removed). Data cleanup was completed with TSL OIM software as described above. Images from EBSD maps were aligned using Avizo for EM™ software.

X-ray diffraction (XRD) measurements on sections of the intercritically annealed material were completed by polishing unmounted samples as stated above for EBSD, but also including a final electro-polishing step to remove all mechanical deformation (15 V for 45 s in a solution of 90% acetic acid and 10% perchloric acid). XRD patterns were collected with Co K $\alpha$  radiation ( $\lambda K\alpha = 0.178897$  nm) using a MeteorOD X-ray diffractometer operated at 40 kV and 30 mA in point focus mode and with a Huber 4-circle + xyz goniometer. The 2 $\theta$  scanning range, 2 $\theta$  step size, count time and rate of sample rotation for each measurement were 20–130°, 0.03°, 20 s/step, and 1 turn/s, respectively. Bruker TOPAS v5.0 was used for Rietveld analysis and included calibration of instrumental broadening with a Si sample, a 4th order polynomial background subtraction and a 6th order preferred orientation correction.

### 2.2.2. BF-TEM and STEM-EDS

Further characterization of the UFG structure utilized bright-field transmission electron microscopy (BF-TEM) and energy-dispersive X-ray spectroscopy performed in the scanning TEM mode (STEM-EDS). TEM-based experiments were performed using an FEI Tecnai Osiris TEM operated at 200 keV and equipped with a quad Super-X detector. Many 3 mm discs were electro-discharge-machined from all material conditions. The 3-mm discs were successively ground to 100  $\mu$ m thickness and electropolished to electron transparency in a Struers twin-jet system with a solution of 5% HClO<sub>4</sub>, 35% [CH<sub>3</sub>(CH<sub>2</sub>)<sub>3</sub>]-O-C<sub>2</sub>H<sub>4</sub>OH, 60% CH<sub>3</sub>OH (by volume) at –30 °C and 15 V. Sections of the intercritically annealed material analyzed by EBSD were used to extract FIB lift-outs for TEM analysis [viewed in the rolling direction] using a FEI Helios NanoLab G3 CX FIB-SEM. With the use of Ga ions, a protective Pt layer was deposited and a trench was bulk milled at 21 nA/30 keV, intermediately milled at 2.5 nA/30 keV, the coupon lifted out and attached to a grid, thinned at 0.79 nA/30 keV and cleaned at 0.07 nA/5 keV. FIB lift-outs mitigate the limitations imposed by preferential electropolishing and reduce the ferromagnetic mass, as compared to self-supporting electropolished 3 mm discs. Bruker Esprit software was used to record 200 keV STEM-EDS hypermaps (spectrum images) of the FIB lift-out specimens with typically 40  $\mu$ s dwell per pixel, 1 nm pixel spacing, 2  $\times$  2  $\mu$ m scanned area and 20 frames for approximately 600 s acquisition. Data processing for each

hypermap data set included background subtraction, peak deconvolution and extraction of normalized wt% elemental maps. Error bars in STEM-EDS measurements are based on 3 $\sigma$  values reported in the Esprit software for a given spectrum deconvolution.

### 2.2.3. APT

For the samples annealed for 0.5 h where the austenite fraction is small, other site-specific FIB lift-outs (5  $\mu$ m  $\times$  20  $\mu$ m  $\times$  5  $\mu$ m) were used to create atom probe tomography (APT) needles based on preceding EBSD scans to identify and capture the ultrafine-grained austenite. The FIB lift-outs were sectioned onto posts and concentrically milled at 2.5 nA/30 keV and then 0.79 nA/30 keV to create a needle geometry, taking care to mill away the protective Pt layer so that the top of the needle is closest to the surface viewed in the EBSD scan. Final cleaning with the FIB at 5 keV and 0.07 nA was used to produce tips of approximately 26 nm radius and 4° shank half angle. These needles were subsequently analyzed in a LEAP 5000 XS APT system and ran until fracture using laser-pulse mode (0.03–0.04 nJ laser energy, 500 kHz pulse frequency, 60 K measurement temperature) and a target detection rate of 1.5% (1.5 ions detected on average for every 100 pulses). Error bars in APT cylinder profiles and proximity histograms are calculated by IVAS software and correspond to the counting error (2 $\sigma$ ).

## 3. Results

### 3.1. Measurements of phase fractions, grain-area and grain morphologies

After cold-rolling, the average Vickers micro-hardness was 390 HV. Measured by dilatometry, the lower and upper temperature bounds of the austenite + ferrite phase field, A<sub>c1</sub> and A<sub>c3</sub>, are respectively 514 °C and 853 °C, whereas Thermo-Calc® simulations predict equilibrium values of A<sub>e1</sub> = 507 °C and A<sub>e3</sub> = 816 °C. Following intercritical annealing of the deformed martensitic microstructure at 585 °C, Thermo-Calc® simulations predict an equilibrium austenite volume fraction of 0.44 and an austenitic RT SFE of 21 mJ/m<sup>2</sup> (see Fig. 1) with an equilibrium austenite composition of Fe-20.8Mn-2.1Al-0.11C (wt%) and an equilibrium ferrite composition of Fe-4.9Mn-3.7Al-0.001C (wt%), as shown in Fig. 2. Methods for thermodynamic SFE calculations are found in Refs. [42–45].

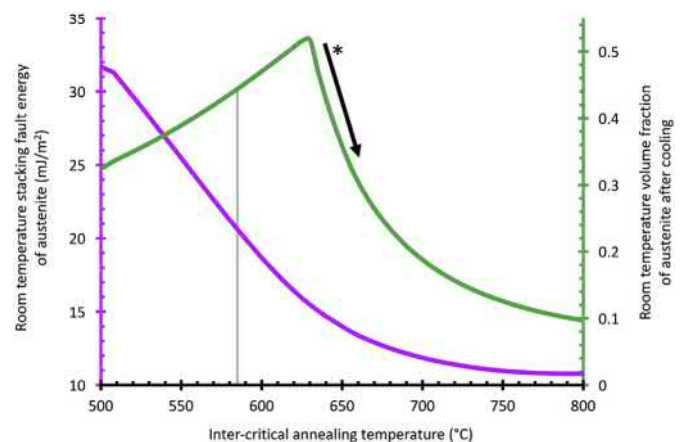


**Fig. 1.** Thermo-Calc® simulations of room temperature stacking fault energy and room temperature volume fraction of austenite as a function of intercritical annealing temperature for a Fe-12Mn-3Al-0.05C (wt%) steel (585 °C marked by a vertical line). \*Corrections to Thermo-Calc® predictions were introduced to compensate for the formation of athermal martensite during cooling as described in Ref. [9].

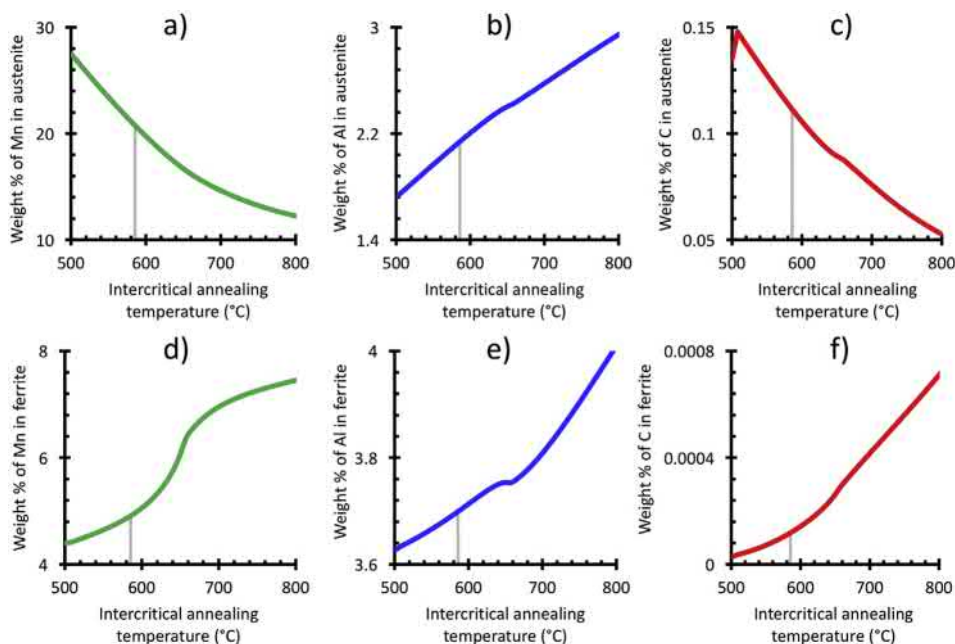


**Fig. 2.** Thermo-Calc<sup>®</sup> simulations of a-c) austenite room temperature composition as a function of annealing temperature and d-f) ferrite room temperature composition as a function of annealing temperature, based on a bulk composition of Fe-12Mn-3Al-0.05C (wt%), where 585 °C is marked by a vertical line.

A deformed and purely martensitic microstructure exists after cold-rolling as indicated by the severe orientation gradients within the martensite (predominantly  $\langle 001 \rangle$  and  $\langle 111 \rangle$ ) indicating a high dislocation density and the absence of any austenite (see Fig. 3a and Fig. 3d). However, some grains experience less deformation and rotation as compared to others. After intercritical annealing the cold-rolled material for 0.5 h at 585 °C, there is a heterogeneous distribution of ultrafine-grained reverted austenite (see Fig. 3b), which indicates that not all nucleation sites have completely developed after annealing for 0.5 h at 585 °C. After increasing annealing time to 8 h, a significant amount of austenite is present throughout the microstructure (see Fig. 3c) and is still ultrafine in size. Prior austenite grains transform to martensite packets (regions within a prior austenite grain formed on different habit planes) during cooling, which are subsequently classified into blocks of multiple variants that are created from the same habit plane [46–49]. During cold rolling, the packets elongate and rotate toward preferred orientations, creating boundaries that are extremely high angle in nature. Boundaries of interest are pictorially represented in Fig. 3f to highlight the presence of a recovered martensitic microstructure after 8 h of annealing. The regions that resemble prior austenite boundaries and block boundaries are likely areas that did not experience as much deformation during cold-rolling.

The XRD profile of the cold-rolled material (see Fig. 4a) indicates a strongly textured martensitic microstructure, as expected for a cold-rolled material prior to annealing steps. In powder-XRD measurements, the  $\{200\}$  planes have a peak intensity of 11% (compared to  $\{110\}$  planes deemed as 100%) when measured for pure ferrite [50]. However, in the cold-rolled martensitic microstructure, the  $\{211\}$  and  $\{200\}$  peak intensities are approximately 15% greater than the  $\{110\}$  peak intensities (consistent with EBSD results), therefore indicating a strong texture in the microstructure. After intercritical annealing for 48 h at 585 °C, austenite peaks appear with strong intensity as expected, but the  $\{211\}$  and  $\{200\}$  peak intensities of the ferrite/recovered  $\alpha'$ -martensite are still greater than the  $\{110\}$  peak intensities (see Fig. 4b). Based on a comparison between XRD texture measurements and EBSD IPF

maps, most of the relatively coarse-grained microstructure observed after 8 h annealing (see Fig. 3c/f) strongly resembles the cold-rolled microstructure of deformed  $\alpha'$ -martensite. XRD measurements for all annealing times (0.5, 8 and 48 h) show no evidence of  $\epsilon$ -martensite peaks.

Increased annealing from 0.5 h to 48 h increases the austenite volume fraction from 3 to 40% (see XRD results in Table 1) and average grain area of reverted austenite from  $0.07 \mu\text{m}^2$  to  $0.68 \mu\text{m}^2$  (see Table 1). Grain-area (rather than grain diameter) measurements provide a better choice for elongated or rod-like grains whereas diameter is best for equiaxed grains. Grain tolerance angle for grain-area calculations used a standard  $5^\circ$  value, which in some cases might not capture some of the low-angle lath boundaries in martensite. Nevertheless, the combined grain area of ferrite and recovered  $\alpha'$ -martensite decreases with increasing annealing time from 0.5 h to 8 h, indicating more austenite reversion and the formation of UFG ferrite (which consumes some of the parent  $\alpha'$ -martensite). However, the average grain area of ferrite and  $\alpha'$ -martensite increases slightly from  $79$  to  $95 \mu\text{m}^2$  when increasing annealing time from 8 to 48 h. This is likely an indication that after annealing for 8 h, formation of UFG ferrite is near completion and traditional growth processes dominate. However, just the average grain area of ferrite and  $\alpha'$ -martensite does not reveal the full picture. Rather, the distributions of each grain area for each phase at a given annealing time give more insight into the reversion process.

The cold-rolled material, composed entirely of deformed  $\alpha'$ -martensite, exhibits a monomodal distribution in grain area, (see Fig. 5a), with a sharp peak at  $578 \mu\text{m}^2$  and an average of  $635 \mu\text{m}^2$ . After intercritical annealing for 8 h at 585 °C, the same sharp peak in grain area shifts from  $578$  to  $79 \mu\text{m}^2$  (see the triangle in Fig. 5b for all phases present and Fig. 5d for only  $\alpha$ -Fe phases). Other peaks in grain area are observed in Fig. 5b. Specifically, for the distribution of only  $\alpha$ -Fe phases observed after 8 h of annealing (see Fig. 5d), a smaller peak at  $3.6 \mu\text{m}^2$  indicates the formation of fine-grained ferrite. As seen in Fig. 5c, the austenite grain area distribution after 8 h of annealing has an average grain area of  $0.46 \mu\text{m}^2$ , which is significantly smaller than the mode indicated for FG ferrite.

Fig. 6 highlights the early stages (after annealing for 0.5 h) of

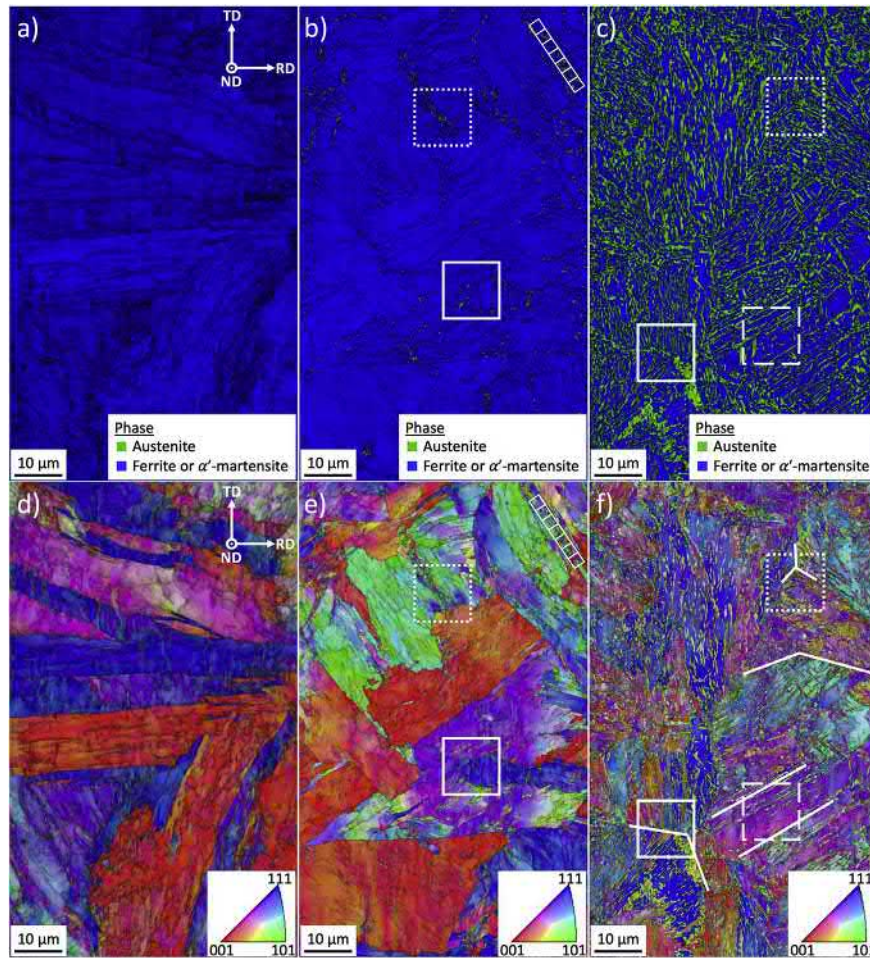


**Fig. 3.** EBSD maps of a-c) image quality and phase, plus d-f) image quality and orientation for the Fe-12Mn-3Al-0.05C (wt%) steel subjected to the following conditions: a/d) cold-rolled, b/e) cold-rolled then annealed for 0.5 h at 585 °C and c/f) cold-rolled then annealed for 8 h at 585 °C. Square boxes indicate regions of interest. f) Annotations help emphasize the appearance of a prior-austenite triple-point (three intersecting lines), packet boundaries (obtuse angle formed by two lines) and block boundaries (two parallel lines).

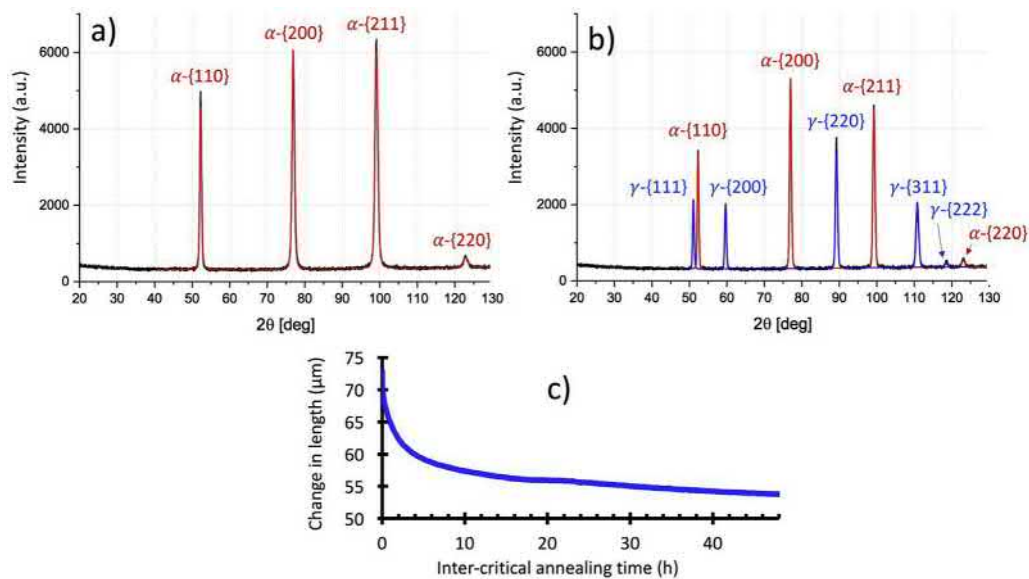


**Fig. 4.** XRD measurements [with a Cobalt X-ray source] of a) the cold-rolled material and b) a sample intercritically annealed for 48 h at 585 °C. c) Dilatometer measurements of the Fe-12Mn-3Al-0.05C (wt%) steel intercritically annealed at 585 °C for 48 h.

**Table 1**  
Austenite volume fraction measured with XRD and EBSD, plus grain areas measured with EBSD for separate annealing times at 585 °C.

Annealing time (h)	Austenite content measured by XRD (%)	Austenite content measured by EBSD (%)	Average austenite grain area measured by EBSD ( $\mu\text{m}^2$ )	Average ferrite/ $\alpha'$ -martensite grain area measured by EBSD ( $\mu\text{m}^2$ )
0	0	1	0.005	635
0.5	3	2	0.073	492
8	29	35	0.458	79
48	40	37	0.678	95

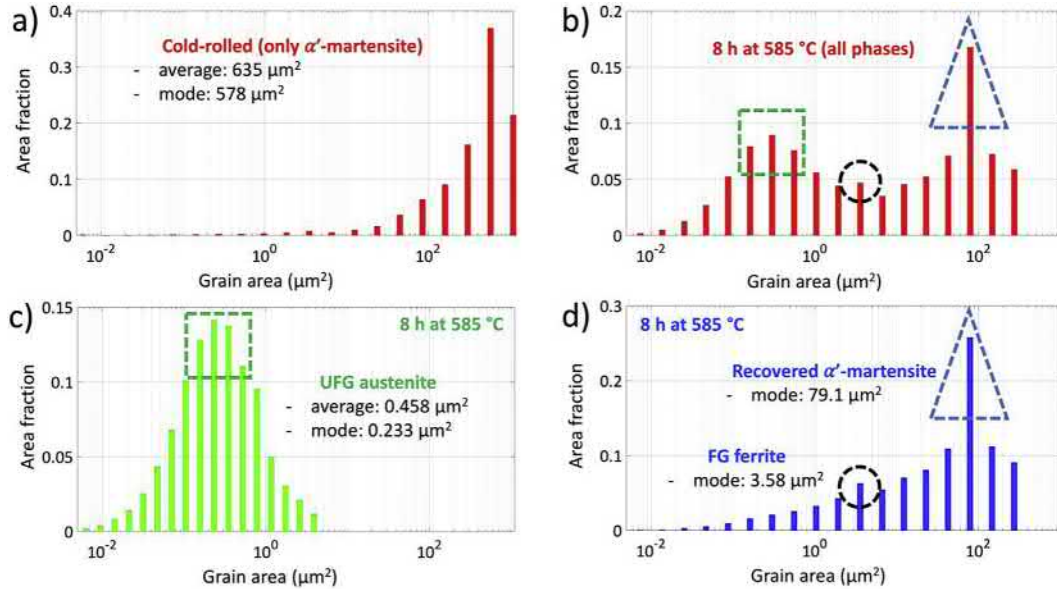


**Fig. 5.** Corresponding grain area distributions, (x-axis plotted in log scale), of a) the cold-rolled martensitic microstructure produced by cold-rolling, b) all phases present after intercritical annealing for 8 h at 585 °C and the differentiated grain areas for given phase fractions of c) ultrafine-grained (UFG) austenite, plus d) coarse-grained recovered  $\alpha'$ -martensite and fine-grained (FG) ferrite. For reference, the square, circle and triangle in b) correspond to the differentiated modal distributions in c) and d).

indirect competition between martensite recovery, martensite recrystallization to create UFG ferrite and the reversion process that creates UFG austenite. For a larger perspective, Fig. 3d–e compares the inverse pole figure (IPF) orientation maps of the microstructure before and after annealing for 0.5 h and indicates that the textured parent martensitic microstructure remains. A characteristic feature of  $\alpha'$ -martensite recovery is a decreased dislocation density, reflected by a decrease in kernel average misorientation (KAM). A majority of the annealed microstructure has a similar grain area to the parent cold-rolled microstructure, but the grains have a lower dislocation density. Average values of between 0° and 0.875° KAM measured by EBSD for  $\alpha$ -Fe phases indicates a high value of 0.44° in the cold-rolled condition, but a decrease to 0.38° after 0.5 h of annealing and 0.37° after 8 h of annealing. The full width at half maximum of the KAM distribution is greatest in the cold-rolled distribution (not shown here) and generally decreases with an increase in annealing time. Fig. 6b and e reveal the presence of ultrafine ferrite grains, which provides evidence that in some cases the  $\alpha'$ -martensite not only recovers, but also forms UFG ferrite. Finally, in the same outlined regions, Fig. 6c and f reveal ultrafine grains of austenite, notably in locations neighboring the ultrafine ferrite grains. This confirms that the reversion process of UFG austenite has begun after annealing for only 0.5 h. An overall observation in Fig. 6 is that nucleation of equiaxed austenite can occur at high-angle boundaries within a parent  $\alpha'$ -martensite packet (see Fig. 6i) and potentially also at newly formed UFG ferrite grain boundaries (see Fig. 6b–c), while rod-like/plate-like austenite grains form at block and lath boundaries (see Fig. 6f).

As seen in Fig. 3c/f, all parent grains (what were the cold-rolled

$\alpha'$ -martensite grains) show evidence of austenite reversion after 8 h of annealing. The outlined area in Fig. 7a–c is likely a triple-point of prior austenite grains (see Fig. 3f for a better perspective) created during the early homogenization step of the thermo-mechanical processing when austenite is the only stable phase. Importantly, this area shows that austenite grains reverted near a triple-point of the prior austenite are randomly oriented, as seen in the IPF map in Fig. 7c. Also, Fig. 7c shows that most of the UFG austenite near what is presumed to be the prior austenite grain boundary (a triple-point as shown in Fig. 3f) is relatively equiaxed in shape and more notably, Fig. 7a–b provides evidence that UFG ferrite is present near the relatively equiaxed and randomly oriented UFG austenite. Fig. 7f shows austenite reverted in the middle of a parent  $\alpha'$ -martensite block, specifically at a lath/sub-block boundary. The austenite morphology appears less equiaxed in shape and less randomly oriented than that shown in Fig. 7c. Fig. 7f displays some rod-shaped austenite grains, whereas other austenite grains are elongated grains strung together, both of which can be distinguished by the location of grain boundaries in Fig. 7d. Fig. 7d–f provides no evidence of UFG ferrite (recrystallization of the parent  $\alpha'$ -martensite) within this specific martensite block. Further, Fig. 7g–i highlights an area of two different martensite packets (see lower magnification perspective in Fig. 3f) with differing geometrical lath alignment (vertical and inclined), which reveals agglomerated austenite orientations as evidenced by similar orientation (near  $\langle 110 \rangle$ ). There are many lamellar austenite grains oriented in the same direction, but also a group of relatively equiaxed austenite grains with the same orientation and low-angle austenite-austenite grain boundaries. An overall observation noted in Fig. 7 is that all

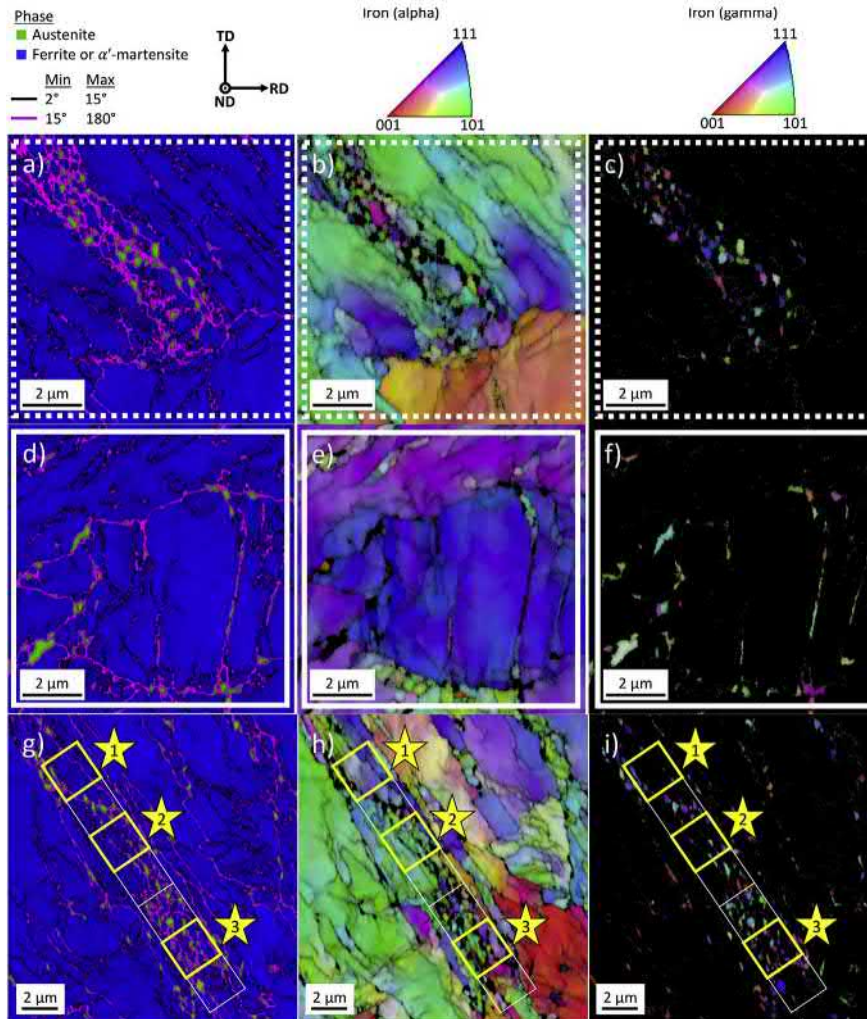


**Fig. 6.** Outlined regions in Fig. 3b/e (Fe-12Mn-3Al-0.05C (wt%) steel annealed for 0.5 h at 585 °C) are shown in greater detail using separate maps for a/d/g) image quality, phase and grain boundaries, b/e/h) image quality and ferrite/ $\alpha'$ -martensite orientation and c/f/i) image quality and austenite orientation. g–i) The location of a site-specific FIB lift-out. The yellow boxes labeled with stars 1–3 denote the approximate location of atom probe needles. (For interpretation of the references to colour in this figure legend, the reader is referred to the Web version of this article.)

dissimilar phase boundaries (austenite–ferrite or austenite–martensite) are high angle in nature ( $15^\circ$  misorientation or greater). Further, boundaries between agglomerated austenite grains (Fig. 7g–i) range from low-angle ( $x < 15^\circ$ ) to high-angle ( $x > 15^\circ$ ). Finally, most boundaries between ultrafine-grained ferrite and the parent  $\alpha'$ -martensite are low angle.

Fig. 8a shows a 3D reconstruction from EBSD orientation maps (based on an acquisition parallel to the rolling direction) for all phases present in the microstructure annealed at 585 °C for 8 h. These measurements allow for a better understanding of the morphology of all phases present at this near-equilibrium state. The entire 3D FIB-EBSD data set includes 109 slices, but the first 95 slices, corresponding to 4.7  $\mu\text{m}$  of material along the rolling direction, are shown in Fig. 8a–b. Fig. 8b displays only the  $\alpha$ -Fe phases from nearly the same reconstructed volume (UFG ferrite and recovered  $\alpha'$ -martensite) for a slightly clearer perspective. Fig. 8a–b also confirms the presence of recovered parent  $\alpha'$ -martensite as well as some parent  $\alpha'$ -martensite laths/sub-blocks, which are low-angle as compared to packet boundaries [51]. In many cases, the UFG ferrite neighbors both parent- $\alpha'$ -martensite boundaries and UFG austenite grains (black pixels in Fig. 8b). Fig. 8c–d clearly demonstrates the existence of multiple UFG austenite

morphologies including rod-like, plate-like, equiaxed grains and equiaxed grains of similar orientation strung together (like a necklace). Fig. 8c shows a smaller volume of only austenite extracted from within the first 95 slices. These equiaxed austenite grains originate from a volume near the packet boundary as indicated with solid lines in Fig. 8a. Fig. 8d shows a small volume of only austenite extracted from slices 86–109, which originates within the  $\langle 101 \rangle$  oriented packet closest to the reader's field of view. Specifically, the arrow in Fig. 8d corresponds to a similar location as denoted by an arrow in Figure S 1b, which shows that the elongated austenite grain forms along a low-angle lath/sub-block boundary. Further inspection of the 3D morphology of this austenite grain pointed to in Fig. 8d/Figure S 1b reveals a plate-like morphology (see supplementary video).

Supplementary video related to this article can be found at <https://doi.org/10.1016/j.actamat.2019.01.003>.

### 3.2. Measurements of chemical compositions in samples annealed for 0.5 h

In the case of samples annealed for 0.5 h (only ~3% volume fraction of austenite present), a site-specific FIB lift-out based on an

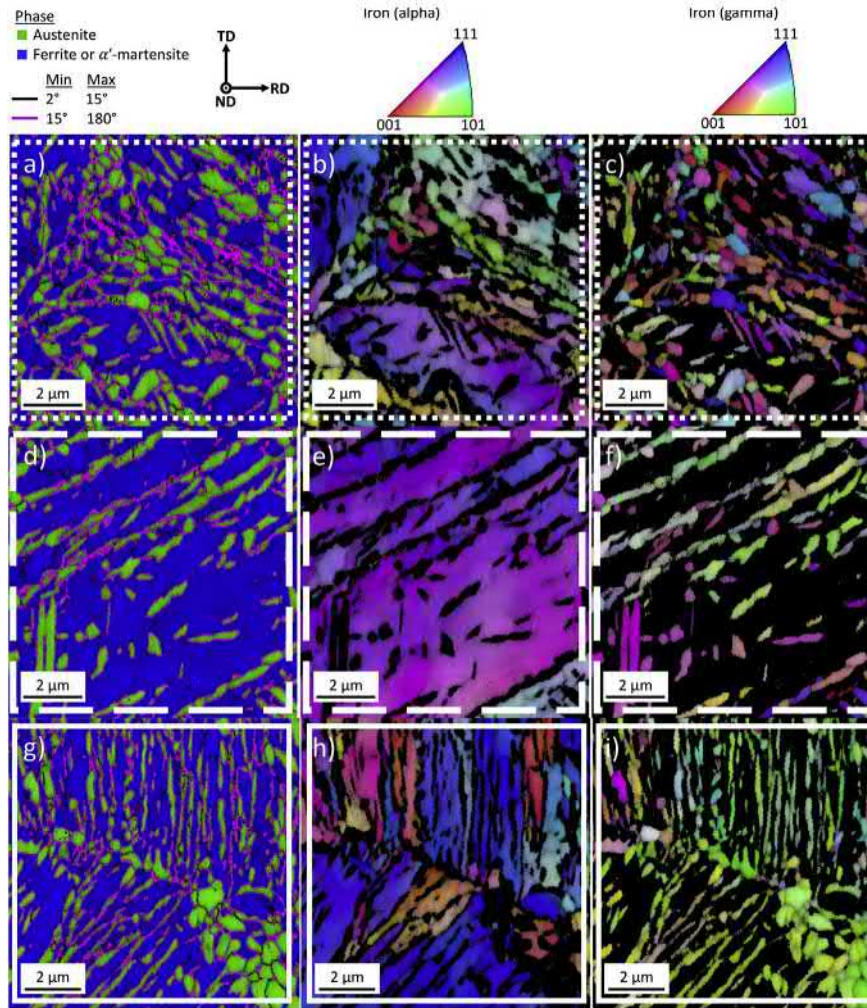


**Fig. 7.** Outlined regions in Fig. 3c/f (Fe-12Mn-3Al-0.05C (wt%) steel annealed for 8 h at 585 °C) are shown in greater detail using separate maps for a/d/g) image quality, phase and grain boundaries, b/e/h) image quality and ferrite/ $\alpha'$ -martensite orientation and c/f/i) image quality and austenite orientation.

EBSD scan was necessary during APT sample preparation to capture the early stages of austenite reversion. Fig. 6g–i identifies a row of locations containing UFG austenite, which is ideal for a FIB lift-out. In many of these locations, but not all, equiaxed UFG ferrite neighbors the equiaxed UFG austenite.

The APT results in Fig. 9a–d correspond to the location denoted by star-1 in Fig. 6g–i. Fig. 9a shows an atom map of Mn with 14 at.% Mn iso-concentration surfaces that in the top part correspond to linear defects such as Mn-decorated dislocations along a cell boundary as well as a Mn-rich particle. The volume with decorated linear defects refers to the recovered martensitic microstructure, as is consistent with the needle location denoted in Fig. 6g–i (star-1). Near the austenite interfaces, there is a Mn-depleted zone in the martensitic grain (Fig. 9c) and no Mn-decorated dislocations are present (Fig. 9a). The length of the Mn depletion zone (2D distance measured away from the austenite interface) varies with boundary curvature in that it is notably thin (approximately 10 nm) near the curved boundary and thicker (approximately 40 nm) near the triple-junction. Analysis of detector hit maps and spatial distribution profiles show differing crystallographic poles in the upper martensitic grain and lower ferritic grain (Fig. 9a–b). Detector hit maps show the locations of ions that are measured with a position-sensitive detector after the ions have passed through the local electrode (following a laser pulse in this case). The detector hit

maps shown in this work are based on the recorded positions of approximately 5 million ions. Spatial distribution profiles shown in this work are amplitude vs. distance plots of local regions in a detector hit map that correspond to a pole such that the spacing between peaks and valleys correspond to a given crystallographic plane. A more detailed description is provided in Ref. [52].

A field factor of 2.65 and image compression factor of 1.3 is used in the atom probe reconstruction algorithm to match the {110} ferrite plane spacing as shown in the spatial distribution map in Fig. 9b. Note that the {110} pole in ferrite gives the best resolution in lattice planes owing to the largest d-spacing in the body-centered cubic (BCC) crystal structure. This consideration gives certainty about the {110} pole identification in the detector map of slice 3 (see Fig. 9a). Also, the appearance of a {110} pole in the detector map as a round low intensity spot is consistent with the following data shown in Fig. 13 and with literature [53]. Further details of the crystallographic analysis procedure are detailed in Ref. [54]. These crystallographic poles (unknown high-index and known {110} poles) indicate that the lower ferritic grain differs significantly in crystallographic orientation as compared with the upper martensitic grain. Given the curvature of the only visible interface of the lower ferrite grain and the proximity to two triple junctions (white arrows in Fig. 9c), it likely corresponds to UFG ferrite.

In the bottom part of the reconstruction, the Mn iso-

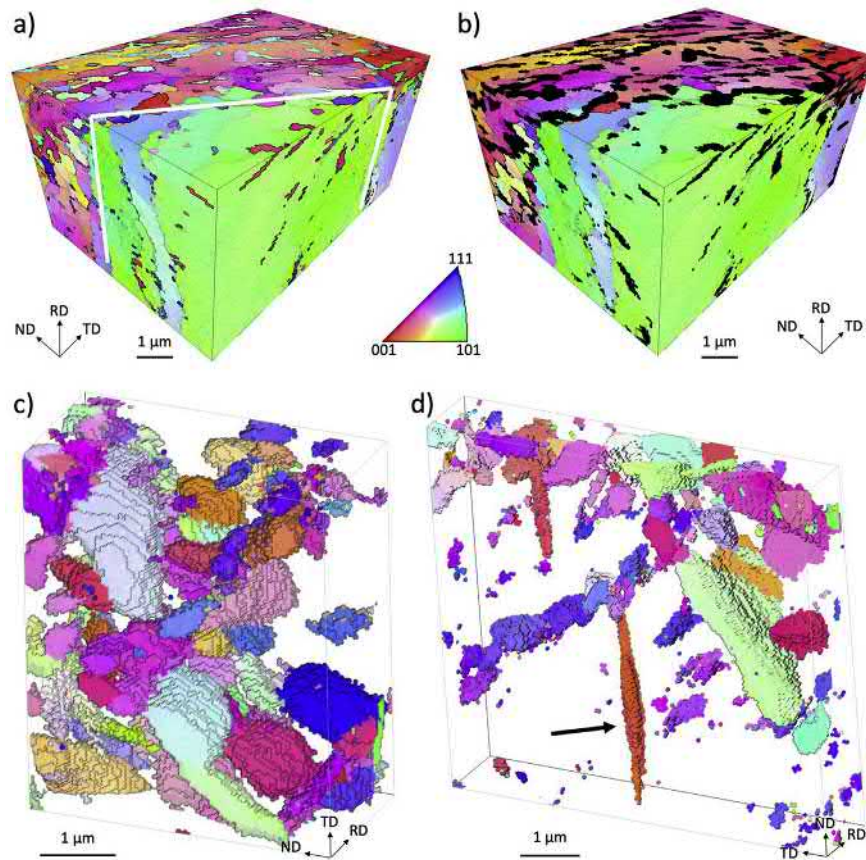


**Fig. 8.** 3D EBSD measurements for Fe-12Mn-3Al-0.05C (wt%) steel annealed for 8 h at 585 °C a) shows the 3D reconstruction for all phases present (orientations are based on inverse pole figure maps - viewed in the rolling direction) and solid white lines indicate an approximate location of a packet boundary. b) Austenite removed from nearly the same reconstruction to highlight the locations and 3D nature of UFG ferrite and recovered parent  $\alpha'$ -martensite. The reconstructed EBSD maps in a-b) are based on 95 FIB slices (a dimension of 4.7  $\mu\text{m}$  for the rolling direction). c-d) Smaller volumes of only austenite aid in visualization of the multiple morphologies. The black arrow in d) indicates an austenite grain that is plate-like (see supplementary video for morphology and Figure S 1b for approximate location in volume).

concentration surfaces envelop two Mn-enriched austenite grains. Fig. 9c–d reveals that in the bottom austenite grain the locations of Mn and C enrichment are mostly the same which indicates co-partitioning from  $\alpha'$ -martensite to austenite. In addition, only one boundary of three at the upper triple-junction is carbon-enriched to approximately 2 at.% (black arrow in Fig. 9d). The C-enriched portion of this interface is extremely flat whereas the curved portion of the interface does not show any C enrichment, which is important to note since boundary curvature usually indicates higher mobility. The lower triple junction also shows evidence of C enrichment, but the lower boundary of three is not completely visible as this volume was not captured in the APT measurements (the curvature at the bottom of the APT needle only indicates the end of the reconstruction). Further, Fig. 9c–d indicates that the austenite reversion process in this ultrafine Mn-enriched grain is not equilibrated as evidenced by the concentration variations seen in the normalized at.% maps within the austenite grains. Analysis of a FIB lift-out (see Fig. 9e–f) using STEM-EDS provides complementary results with quantitative composition maps. The results in Fig. 9f indicate some variability in Mn concentrations (23–34 wt% Mn) for observed austenite nuclei, but the larger austenite grains are consistent with the size and morphology of austenite grains observed in EBSD scans of a different region in the same bulk sample (see Fig. 6c/f). Some of the Mn-enriched regions in Fig. 9f are so small that they may be embedded in the sample and so their apparent Mn content may be an underestimate due to overlap with the surrounding microstructure. Nevertheless, Fig. 9f indicates

instances of austenite grains with near-equilibrium concentrations of Mn. In the context of Thermo-Calc<sup>®</sup> predictions (Fe-12Mn-3Al-0.05C wt% bulk composition and annealed at 585 °C using the TCFE7 database), equilibrated Mn concentrations in austenite should be approximately 22 wt% Mn. Finally, most of the austenite grains are surrounded by zones in the martensite depleted in Mn to concentrations as low as approximately 6 wt% Mn, whereas the rest of the martensite possesses a higher concentration (10.5 wt% Mn), which is close to the bulk Mn composition (12 wt%). Note that this observation is in excellent agreement with the Mn depleted zone revealed by APT measurements.

Fig. 10a is a BF-TEM image of an electropolished specimen of material annealed for 0.5 h at 585 °C and shows elongated regions (indicated with white arrows) that show evidence of preferential attack during the electropolishing process. Previous work on these materials has unequivocally demonstrated that, for the electropolishing conditions employed here, austenite is strongly preferentially removed [55]. Therefore, although only circumstantial, it is highly likely that the elongated regions marked with white arrows were regions of austenite. Other areas in Fig. 10a, however, reveal similarly elongated particles that were not preferentially electropolished and exhibit dark contrast as indicated by the black arrows. Fig. 10b shows them in greater detail (but with reversed contrast) in the high-angle annular dark-field STEM image. Fig. 10c shows spectra extracted from the STEM-EDS hypermap for two areas, spot 1 on the particle and spot 2 in the nearby matrix. The spot-1 spectrum shows a clear C peak, intense Mn peaks and no

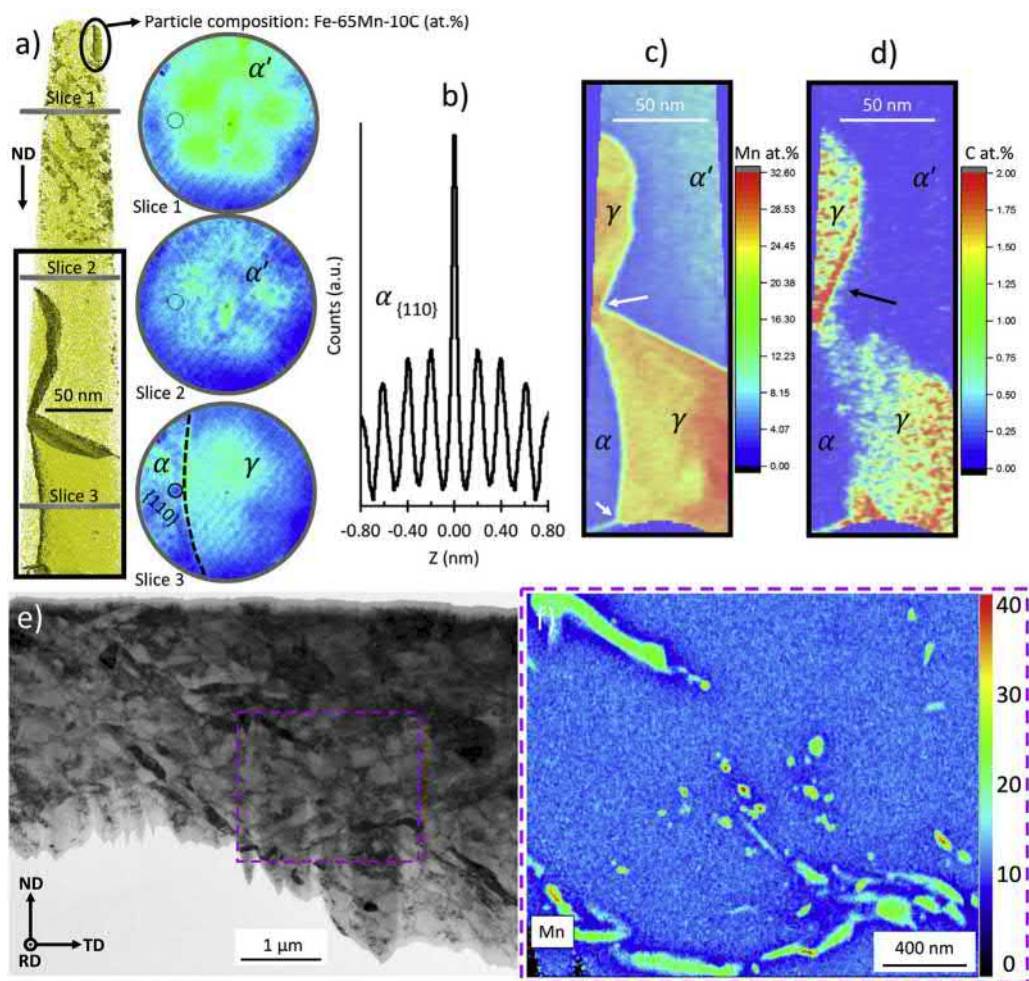


**Fig. 9.** a) Mn atoms and 14 at.% Mn iso-concentration surfaces displayed from an APT run of  $1.5 \times 10^8$  ions from a sample annealed for 0.5 h at 585 °C. The APT needle location is from the star-1 position in Fig. 6g–i. Slices 1–3 correspond to detector hit maps (field of view is 60 nm in diameter) and provide a guide for interpreting unknown high-index (dashed circle) and indexed (bolded solid circle) crystallographic features in volumes of approximately 5 million ions. b) A spatial distribution map identifies a {110} pole in the lower  $\alpha$  grain. The quantitative c) Mn and d) C maps of two austenite grains with triple-junctions (white arrows) highlight co-partitioning, concentration gradients, Mn depletion zones and a C-enriched interface. e) A BF-TEM image of a FIB lift-out viewed in the rolling direction denotes the location of STEM-EDS mapping. f) The quantitative Mn elemental map (in wt%) indicates a dispersion of Mn-enriched particles and Mn depletion zones near austenite grains.

detectable intensity for the Al peak. In the spot-2 spectrum the Fe peaks are much larger than the Mn peaks, there is a small but clear Al peak and no detectable C peak. The absence of C for the matrix spectrum adds confidence that the C signal from the particle is real and not due to an artifact, especially specimen contamination.

Depictions of the EDS results in the form of quantitative composition maps (Fig. 10d–g) indicate that the particles are mixed-metal carbides containing Fe as well as Mn and are not just binary Mn–C particles. Their elongated nature suggests that the carbides have formed along a boundary in the parent microstructure. Other smaller particles near the elongated carbides, as clearly revealed in the Fe and Mn maps (Fig. 10d–e), have much lower apparent carbon contents and contain Mn concentrations much closer to those predicted for equilibrium austenite. However, the particles are much more likely to be embedded within the matrix and to not extend all the way through the TEM specimen, which would of course result in lower Mn and C signals. Fig. 10h is a BF-STEM image of an electropolished sample and clearly shows the sub-grain structure of the recovered  $\alpha'$ -martensite in that there are cell-like boundaries with a high density of dislocations that surround regions of smaller grains with a much lower dislocation density. Fig. 10h also shows the presence of preferential

electropolishing (removed austenite) and particles that were not preferentially electropolished. Fig. 10i is a BF-TEM image of a different region in the electropolished sample that highlights the proximity of elongated particles near a boundary.

Fig. 11 depicts an austenite grain near the top of an APT needle and the overall Mn content (Fig. 11b) is close to the equilibrium concentration predicted for austenite by Thermo-Calc<sup>®</sup> simulations for this annealing temperature (22.5 at.% Mn is approximately 22 wt% Mn). No Mn-decorated dislocations are observed within 130 nm of the austenite boundary. Fig. 11b also identifies the location of two triple-junctions between UFG austenite, UFG ferrite and recovered  $\alpha'$ -martensite (marked with solid lines slightly offset from the boundary). Fig. 11c shows a flat interface in between the two triple-junctions that is enriched with C up to approximately 3 at.%. The grain boundaries separating the UFG ferrite grains are also slightly enriched in Mn. The Mn level in the ferritic region is consistent with Thermo-Calc<sup>®</sup> simulations of RT equilibrium ferrite composition (approximately 5 at% Mn) for this annealing temperature (585 °C). Further, those grain boundaries in the ferritic area of Fig. 11b show rather homogeneous Mn distribution which contrasts with the boundaries in the lower part of this APT reconstruction where Mn enrichments are periodically aligned within the

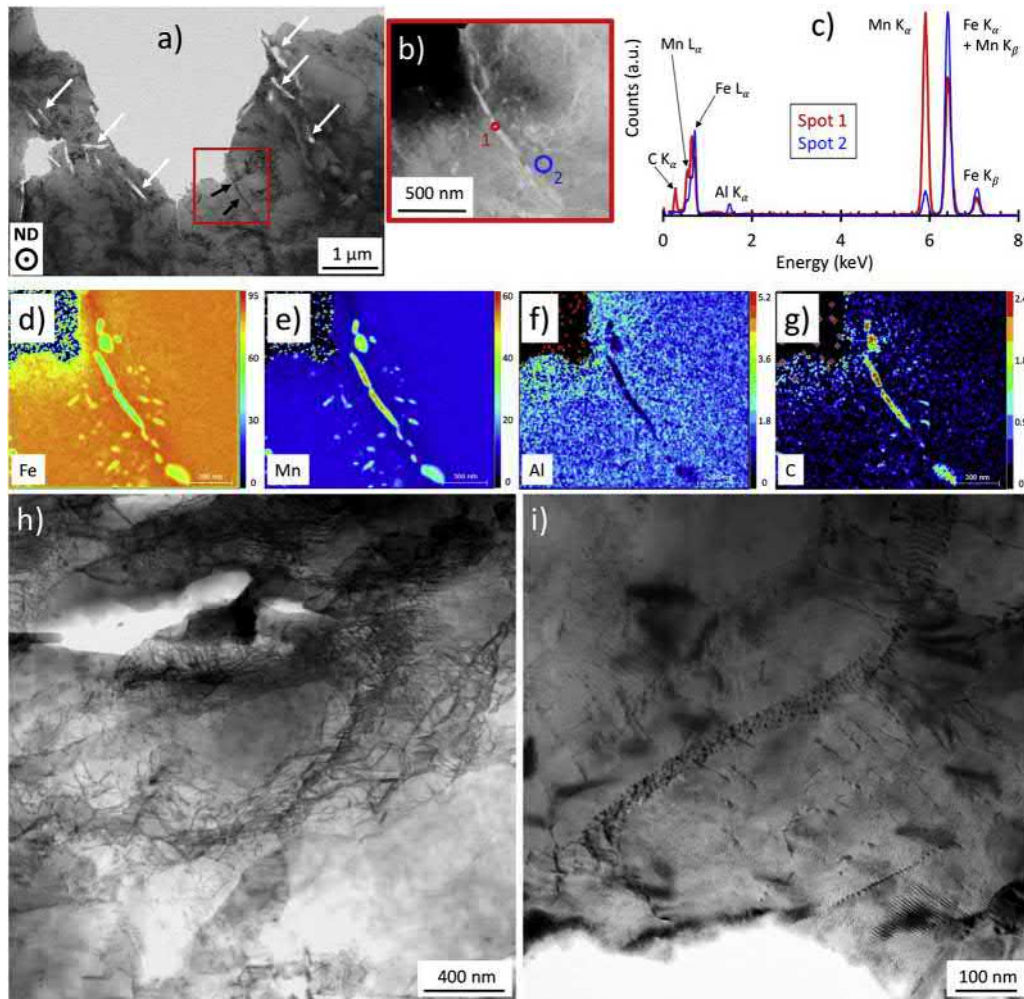


**Fig. 10.** a) BF-TEM image of an electropolished specimen of material annealed for 0.5 h at 585 °C viewed in the normal direction indicating regions of preferential electropolishing (presumably austenite – white arrows) and elongated particles that remain (black arrows in the square). b) High-angle annular dark-field STEM image shows the area mapped by EDS and indicates the locations used to extract from the hypermap c) spectra from the particle (spot 1) and the parent  $\alpha'$ -martensite (spot 2). Quantitative composition maps extracted from the EDS hypermap (spectrum image) are shown for d) 0–95 wt% Fe, e) 0–60 wt% Mn, f) 0–5.2 wt% Al and g) 0–2.4 wt% C. h) BF-STEM and i) BF-TEM images highlight the sub-grain and dislocation structure of the recovered  $\alpha'$ -martensite and particle presence near boundaries.

boundary plane along rods that resemble individual dislocation cores. The first case relates to a high angle grain boundary (evidenced with analysis of detector hit maps and spatial distribution profiles analogous to those in Fig. 9a), while the latter case corresponds to a low-angle dislocation cell boundary (see Fig. 11f) where the misorientation directly relates to the periodicity of Mn enrichment, i.e. dislocations. Fig. 11d reveals two spherical regions approximately 15 nm in diameter that are in the  $\alpha'$ -martensite near Mn-enriched linear defects. The two regions have C and Mn concentrations far above the values predicted by thermodynamic calculations for the local equilibrium (LE) between ferrite and austenite. Quantitative proximity analysis from the iso-concentration surface shown in Fig. 11e yields a Mn concentration of 60 at.% and a C concentration of 11 at.%.

Another APT reconstruction from the sample annealed for 0.5 h at 585 °C is shown in Fig. 12a in terms of a Mn atom map with 14 at.% Mn iso-concentration surfaces. The top part of the APT reconstruction contains an austenite grain (see Fig. 12b) with a composition close to the equilibrium predicted by Thermo-Calc<sup>®</sup> and less variation in Mn content throughout the grain interior. The bottom boundary of the austenite grain is enriched with carbon up to 1.5 at.%, as indicated in the concentration profile of Fig. 12d. The

position of the austenite grain (top of the needle) is consistent with the location from which the milled FIB post originated (UFG austenite grains near the center of the box denoted star-3 in Fig. 6g–i). Given the parallel and planar orientation of the lath boundaries farther down the APT needle (see Fig. 12a and c) and the linear defects (dislocations) decorated with Mn-enrichment, the base of the needle likely contains four neighboring laths of the recovered parent  $\alpha'$ -martensite. Further analysis of detector hit maps and spatial distribution profiles not shown here also confirms that all four laths possess about the same orientation with only a few degrees misorientation. Note that also the austenite-martensite boundary is approximately parallel to those lath boundaries which might indicate the martensite-martensite interface as a possible austenite nucleation site. From top to bottom, the APT needle in Fig. 12a appears to contain UFG austenite that has a composition of about 20 at.% Mn (reverted austenite) and recovered parent  $\alpha'$ -martensite laths filled with dislocations that are decorated with Mn when they are sufficiently far away from the growing austenite. In the lath closest to the austenite, no Mn-decorated features are observed. The first two martensite-martensite lath boundaries are denoted as “i” and “ii”. The composition profile in Fig. 12d shows that the first two  $\alpha'$ -

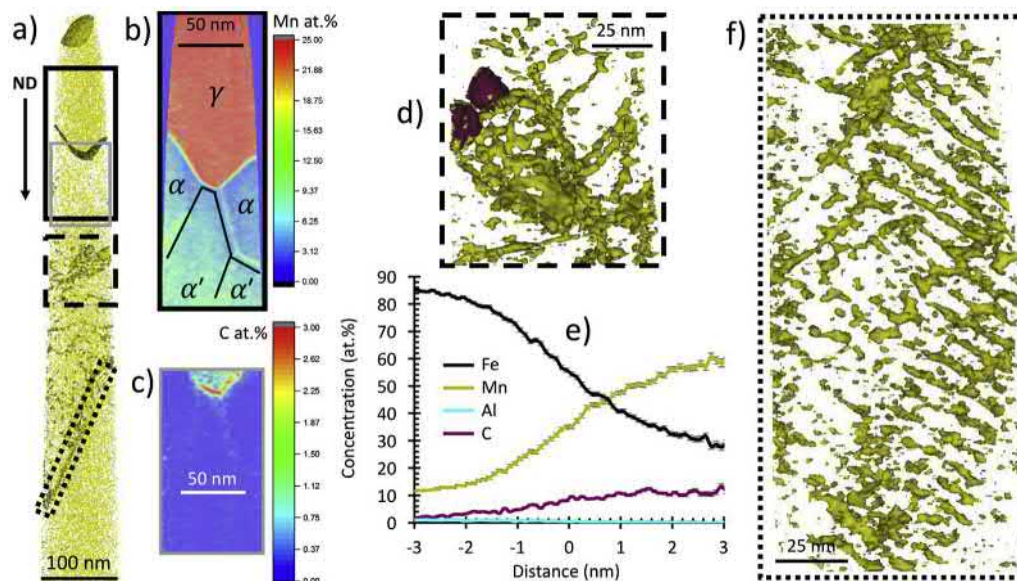


**Fig. 11.** a) Mn atom map and 14 at.% Mn iso-concentration surfaces displayed from an APT run of  $3.6 \times 10^8$  ions from a sample annealed for 0.5 h at 585 °C. The APT needle location is from the star-2 position in Fig. 6g–i b) The quantitative Mn map highlights two triple-junctions between an austenite grain, ferrite grains and recovered  $\alpha'$ -martensite laths. c) The quantitative C map shows C enrichments between the two triple junctions. d) The region marked by a dashed box in a) displays only iso-concentration surfaces of 14 at.% Mn and 8 at.% C and reveals the presence of two Mn- and C-enriched features as seen in e) the composition profile calculated in the form of a proximity histogram (0 nm is the interface defined by the 8 at.% C iso-concentration surface [56]). f) The region marked by a dotted box in a) is rotated to show the low-angle lath boundary composed of Mn-decorated dislocations. All error bars in APT cylinder profiles and proximity histograms are calculated by IVAS software and correspond to the counting error ( $2\sigma$ ).

martensite laths exhibit small enrichments in Mn on an otherwise pronounced gradient in Mn content within 100–150 nm of the austenite. Fig. 12d also shows that the concentration of Mn piles-up at the austenite-martensite interface, after which it decreases by  $\sim 2$  at.% in the first 40 nm away from the interface towards the core region of the austenite grain.

Additionally, simulations were performed using DICTRA (a time- and space-dependent Thermo-Calc<sup>®</sup> diffusion module) to better understand the compositional evolution of austenite. The DICTRA simulations assume a planar cell boundary condition with a width of 300 nm. The simulations were initialized with austenite as an inactive phase, which would be created during the simulation with a critical nucleus composition obtained by the parallel tangent construction [57–59]. The results of the DICTRA simulations in Fig. 12e–f are based on a moving interface of a local equilibrium between austenite and ferrite. The experimentally measured Mn depletion profile in the martensite (Fig. 12d) and that simulated with ferrite DICTRA (Fig. 12e) agree in a general way, although the simulated profile is narrower. Similarly, the simulated C levels in the austenite (Fig. 12f) agree in a general way with those measured experimentally (Fig. 12d). DICTRA simulations also show that the initial austenite composition during early stages of nucleation has a much higher Mn content as compared to equilibrium simulations with Thermo-Calc<sup>®</sup> (see Fig. 12e). Further, the simulations show that as annealing time increases, which moves the austenite-ferrite interface, the C content becomes diluted in the austenite and the Mn content also spatially equilibrates.

### 3.3. Measurements of chemical compositions in samples annealed for 8 h

On a meso-scale, the distribution of austenite grains is widespread throughout samples annealed for 8 h at 585 °C (see Fig. 3c), so the location of a FIB lift-out for APT needles was chosen at random. A consistent feature observed in APT needles from material heat treated for 8 h (see Fig. 13) is an equilibrated Mn content in

the austenite without interface pile-up. However, the experimentally measured Al concentrations in each phase are consistently lower than Thermo-Calc<sup>®</sup> predictions, but the relative comparison between the austenite and ferrite/ $\alpha'$ -martensite in all APT measurements is consistent in that the reverted austenite contains lower concentrations of Al as compared to the ferrite/ $\alpha'$ -martensite. The systematically lower Al content measured with APT might be due to a peak overlap between  $\text{Fe}_{54}^{+2}$  and  $\text{Al}^{+1}$  and is a known issue that has been dealt with for the past few decades [60–62]. Further, a recent study by Dmitrieva et al. [63] mentioned ions that are field evaporated between voltage/laser pulses may lead to error in composition measurement due to preferential field evaporation of elements with lower evaporation fields and is specifically dependent on laser energy.

As depicted in Fig. 13a–c, an APT reconstruction from a sample annealed for 8 h reveals the presence of carbon-enriched interfaces, in this case at one boundary segment from a triple-junction. Detector hit maps in Fig. 13a show that the two parent grains are misoriented by less than a few degrees, which is characteristic of a low-angle lath boundary between two  $\alpha'$ -martensite laths. In each detector map the same four poles ( $\{002\}$ ,  $\{110\}$ ,  $\{112\}$  and another  $\{110\}$ ) are identified which match the expected pole locations for a  $\{112\}$ -oriented BCC-Fe grain. Note that due to the limited detector field-of-view in the atom probe only a  $\sim 30^\circ$  segment around the center axis (in this case close to  $\{112\}$ ) is captured. The austenite-martensite interface evolves at a larger angle from the neighboring low-angle lath boundary.

In Fig. 13d–g, another APT reconstruction reveals an ultrafine austenite grain with an equilibrated Mn concentration of Fe-22.5Mn-0.83Al-0.49C at.%/Fe-22.0Mn-0.4Al-0.11C wt.% that again matches Thermo-Calc<sup>®</sup> simulations. A slight Mn gradient is noted in the first 40 nm of  $\alpha'$ -martensite closest to the austenite boundary (see Fig. 13f). Furthermore, a C-enriched segment is observed at the austenite- $\alpha'$ -martensite boundary (Fig. 13g), especially on the flat segment (the curved portion of the boundary is not as enriched with C). Finally, spatial distributions of the Fe and Mn atoms along

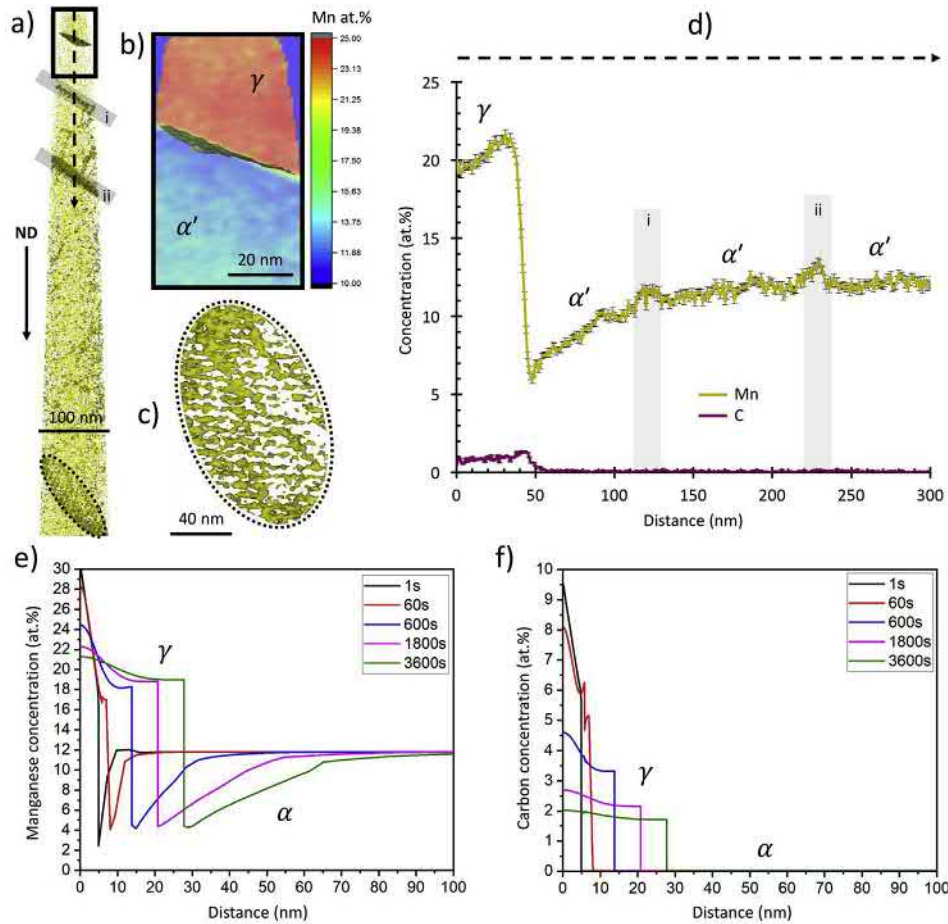


**Fig. 12.** a) Mn atom map and 14 at.% Mn iso-concentration surfaces displayed from an APT run of  $3.7 \times 10^8$  ions from a sample annealed for 0.5 h at 585 °C. The APT needle location is from the star-3 position in Fig. 6g–i b) The quantitative Mn map (with a 14 at.% iso-concentration surface) reveals an austenite grain with a Mn content consistent with equilibrated values as predicted by Thermo-Calc® simulations. c) The oval region marked in a) highlights the low-angle martensitic lath boundaries with Mn decoration. d) The line profile through the upper half of the APT needle indicates a region (free of decorated dislocations) that is increasingly depleted in Mn when approaching the austenite grain and spikes in Mn concentrations (indicated by i and ii) at  $\alpha'$ -martensite lath boundaries. All error bars in APT cylinder profiles and proximity histograms are calculated by IVAS software and correspond to the counting error ( $2\sigma$ ). e–f) DICTRA simulations at 585 °C using an Fe-12Mn-3Al-0.01C (wt%) bulk composition show increased Mn and C concentrations in austenite at early annealing times, co-partitioning of Mn and C and the distance the austenite-ferrite interface has travelled during annealing.

the  $\{110\}$   $\alpha'$ -Fe and  $\{111\}$   $\gamma$ -Fe pole (Fig. 13d–e) show that the C-enriched interface segment is parallel to the  $\gamma_{\{111\}}/\alpha'_{\{110\}}$  planes and also indicates a probable Kurdjumov-Sachs (KS) orientation relationship. By following the same routine for the APT reconstruction as described in Fig. 9, the field factor was tailored such that the  $\{110\}$   $\alpha'$ -Fe plane spacing matches the expected value of 2.03 Å. At the same time, the resulting plane spacing along the same direction in the austenite comes remarkably close to the expected value of 2.08 Å for  $\{111\}$   $\gamma$ -Fe planes. Slight deviations arise from the difference in field evaporation in austenite and  $\alpha'$ -martensite, which changes the field factor across the interface.

In previous work [55], convergent beam electron diffraction (CBED) analysis was successfully applied to electropolished samples annealed for 8 h at 585 °C and confirmed the presence of UFG ferrite in close proximity to UFG austenite. Results of EDS spectrum lines across ferrite and austenite grains in that study [55] yielded Mn contents nearly identical to Thermo-Calc® simulations for austenite and ferrite. In the present work, 2D and 3D EBSD measurements (viewed in the normal and rolling directions) and BF-TEM images (viewed in the rolling direction) reveal various morphologies of austenite (equiaxed and rod-shaped) and such results are consistent with previous work completed using electropolished TEM samples viewed in the normal direction [55]. In both the

previous and current work, the Al content for both the austenite and ferrite/ $\alpha'$ -martensite grains are lower than predicted, but the relative comparison between the two ultrafine grains is consistent with the equilibrium predictions, where reverted austenite contains less Al than ferrite or  $\alpha'$ -martensite. An independent analysis of the bulk composition was completed using acid digestion and indicated the bulk alloy does indeed contain 3 wt% Al. Accurate quantification by EDS of Al in transition metal alloys such as steels is notoriously difficult, primarily because of absorption of the relatively soft Al K X-rays in the sample along the path from the generation point to the detector [64–66]. Schemes for absorption correction have been devised dating from the earliest years of EDS on a (S)TEM [64], but the exact specimen geometry and its orientation to the EDS detector(s) must be known. In practice, a great deal of extra effort is involved and many times is unjustifiable for the problem on hand.

To understand the morphology and composition of UFG austenite viewed in the rolling direction, a FIB lift-out specimen was prepared and analyzed (Fig. 14) and the results complement the observations from EBSD measurements in that various austenite grain morphologies appear, namely equiaxed, equiaxed and strung together, rod-like and plate-like. Also, Mn concentration maps yielded area fractions of 35% austenite (from Fig. 14b), which

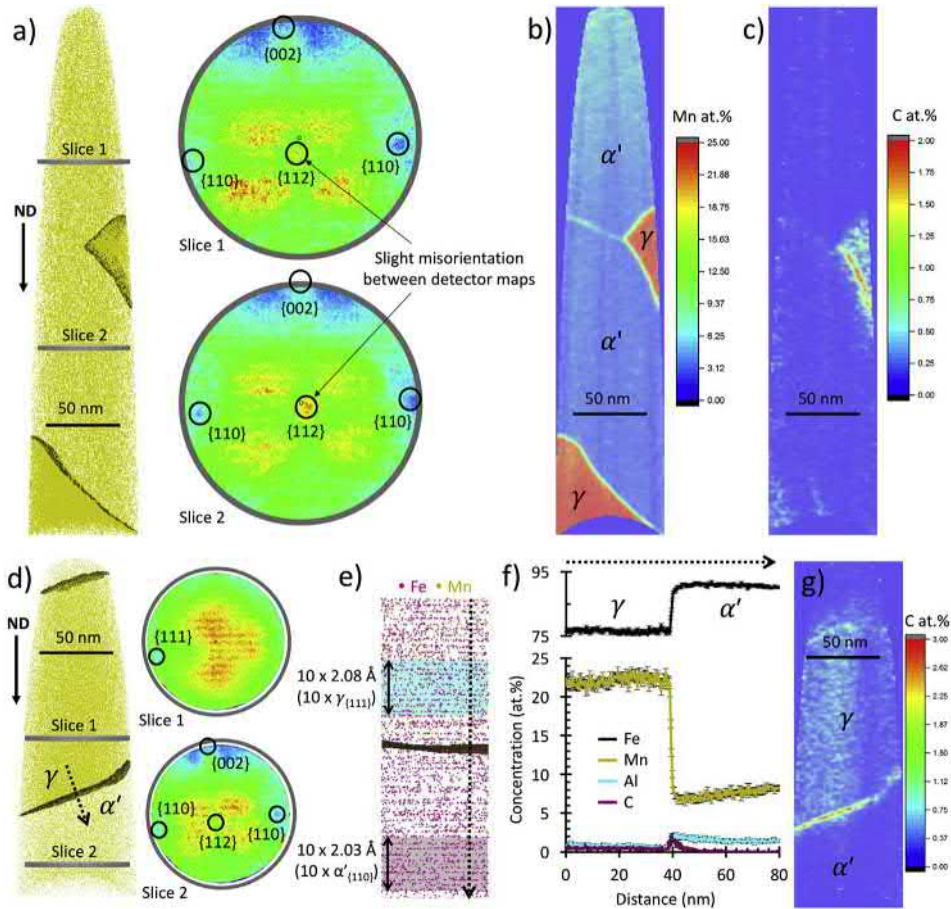


**Fig. 13.** a) Mn atom map and 14 at.% Mn iso-concentration surfaces displayed from an APT run of  $2.7 \times 10^8$  ions from a sample annealed for 8 h at 585 °C. Slices 1 & 2 correspond to detector hit maps (field of view is 60 nm in diameter) each with four identified poles that indicate a low misorientation between the two recovered  $\alpha'$ -martensite laths. The quantitative maps of b) Mn and c) C show evidence of a grain boundary triple-junction and a C-enriched boundary segment. d) Mn atom map and 14 at.% Mn iso-concentration surfaces displayed from an APT run of  $1.5 \times 10^8$  ions from a sample annealed for 8 h at 585 °C. Slices 1 & 2 correspond to detector hit maps (field of view is 60 nm in diameter) with indexed poles. e) A display of Fe and Mn atoms identifies a plane match of {110}  $\alpha'$ -martensite and {111}  $\gamma$ . f) The cylinder profile marked with a dotted arrow in d) provides quantitative compositional analysis across the same boundary. g) A quantitative C map identifies a C-enriched flat segment at the boundary. All error bars in APT cylinder profiles and proximity histograms are calculated by IVAS software and correspond to the counting error ( $2\sigma$ ).

is consistent with the phase fraction measured by EBSD (see Table 1). STEM-EDS scans of a near edge-on austenite- $\alpha'$ -martensite boundary (Fig. 14f) are similar to the equivalent APT results (see Fig. 13e) and show that equilibrated Mn concentrations are observed at a distance of 6 nm or more from the austenite interface. Whereas STEM-EDS offers high-resolution mapping for tens of ultrafine grains at a time in a FIB lift-out specimen, 3-dimensional APT offers improved spatial resolution for measurements of composition profiles across UFG austenite-ferrite boundaries with better detectability and higher accuracy for light elements such as carbon, especially at low concentrations. Finally, most of the microstructure excluding austenite has a Mn composition similar to that of Thermo-Calc® simulations for equilibrated ferrite (approximately 5.5 wt.% Mn) even though many grain morphologies are characteristic of a recovered microstructure.

#### 4. Discussion

##### 4.1. Compositional evolution during austenite reversion

Samples of the Fe-12Mn-3Al-0.05C (wt%) steel annealed for 0.5 h provide great insight into the compositional evolution of the microstructure during intercritical annealing at the given holding temperature in the two-phase region (585 °C). Both APT

measurements and STEM-EDS measurements of local compositions in samples annealed for 0.5 h reveal zones of Mn depletion in the recovered  $\alpha'$ -martensite in the vicinity of reverted ultrafine austenite grains. Based on measurements in Fig. 9c, f, Figs. 11b and 12d, the width of the Mn depletion zone (distance away from the austenite boundary) ranges from 15 to 150 nm. The scatter might arise from local variations in the shape and curvature of the boundary and proximity to triple-junctions. Overall, the DICTRA simulations shown in Fig. 12e are consistent with the experimental observations. Also, APT results from samples annealed for 0.5 h reveal Mn-decorated defects (dislocations networks and low-angle lath boundaries) throughout the recovered  $\alpha'$ -martensite grains (see Figs. 9a, 11a and 11f, Fig. 12a and c), which agrees well with other works on intercritically annealed medium-Mn steels [36,67,68]. Further, recent work by Kwiatkowski da Silva et al. [68] shows that both linear and planar defects can adsorb Mn atoms and form confined spinodal fluctuations which eventually act as nucleation sites for UFG austenite. This phenomenon is consistent with APT results of samples annealed for 0.5 h in this study as austenite nuclei are observed near networks of Mn-decorated dislocations (see Figs. 9a and 11d–e). However, Mn-decoration at defects is absent in the zones of Mn depletion near the austenite boundaries (see Figs. 9a, 11a and 12a). The lack of decoration promotes dislocation annihilation and recovery. The depletion of Mn

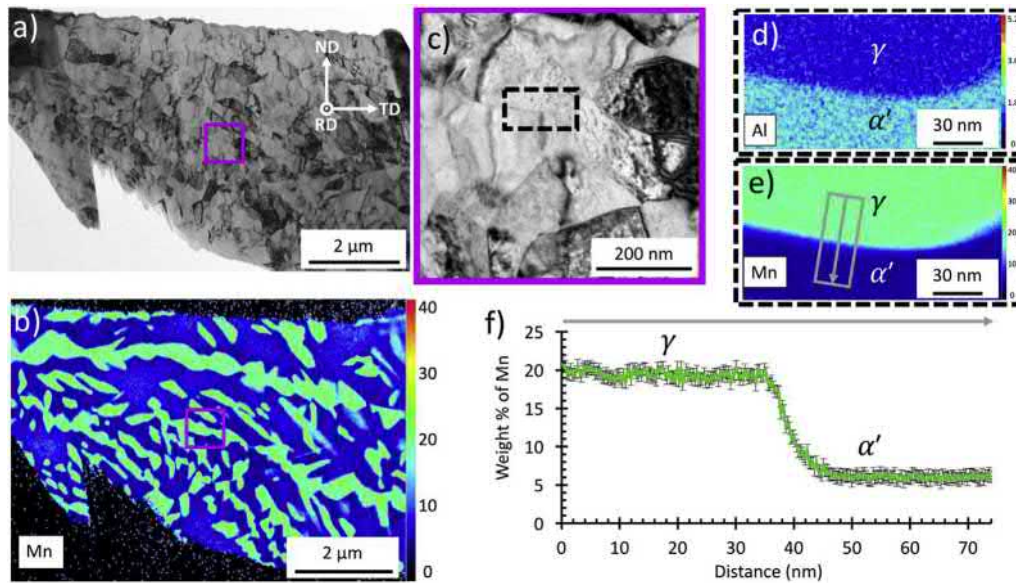


**Fig. 14.** FIB lift-out of a sample annealed for 8 h at 585 °C viewed in the rolling direction, as indicated in a) the BF-TEM image. b) The quantitative Mn elemental map (0–40 wt%) extracted from a STEM-EDS hypermap indicates Mn-enriched UFG phases (austenite) with multiple morphologies of rod-like grains and more equiaxed grains strung together. c) BF-TEM image [location marked in a)] shows a near edge-on boundary between austenite and recovered  $\alpha'$ -martensite, as revealed by the d) 0–5.2 wt% Al and e) 0–40 wt% Mn maps. The arrow in e) denotes the location of f) the Mn (wt %) profile across the boundary. Error bars in STEM-EDS measurements are based on  $3\sigma$  values reported in the Esprit software for a given spectrum deconvolution.

near the austenite interface may also increase the grain boundary mobility in the  $\alpha'$ -martensite and favor the recrystallization of cold-rolled  $\alpha'$ -martensite to form UFG ferrite. Recrystallization requires only short-range diffusion of Fe atoms to form new ferrite grains, but the Mn atoms provide a solute drag effect on grain boundaries and potentially hinder ferrite recrystallization away from austenite grains where the Mn concentration is still elevated in martensite. Overall, the Mn content of UFG austenite is 22.5 wt% and thereby near to equilibrium after 8 h of annealing.

Particles and/or austenite nuclei were identified with STEM-EDS and APT near networks of Mn-decorated defects (dislocation networks and low-angle lath boundaries) in samples annealed for 0.5 h at 585 °C (see Fig. 9a, f and 11d–e). Such nuclei possess Mn and C concentrations (60/64 at.%/wt% Mn and 10/2.4 at.%/wt% C) far above the values predicted by thermodynamic calculations for the local equilibrium between ferrite and austenite. However, these Mn-rich and C-enriched particles are not present after 8 h of annealing, indicating low thermodynamic stability at equilibrium. Specifically, Thermo-Calc<sup>®</sup> simulations indicate that there is a low chemical driving force for the formation of stable carbides in this alloy due to the low C content (<0.06 wt%). For example, Thermo-Calc<sup>®</sup> predicts a cementite mole fraction of 0.001 with an equilibrium phase composition of Fe-70Mn-6C (wt%) for an intercritical annealing temperature of 500 °C, but no cementite stability above 500 °C. However, the experimental results from TEM convincingly support the presence of carbide particles in the electropolished samples annealed at 585 °C for 0.5 h (Fig. 10a–g). Although it is difficult to arrive at a confident quantitative composition from EDS data because of the strong absorption of the soft C X-rays in the specimen (to a much greater extent than for the Al X-rays discussed above in section 3.3), the absence of preferential etching attack (Fig. 10a–b) and substantial C contents (Fig. 10c,g) indicate a sound identification of carbides. Further, the elongated nature of those carbide-like particles indicates nucleation at an interface in the parent microstructure, such as a lath boundary or cell boundary, which is characteristic of  $M_{23}C_6$  carbide formation [69,70]. Since the metal (M) in  $M_{23}C_6$ ,  $M_6C$  and  $M_3C$  carbides can be either Mn or

Fe, it is likely that the Mn- and C-enriched particles are mixed-metal carbides and this is supported by the composition measurements. Further yet, STEM-EDS results from a FIB lift-out extracted from a sample annealed for 0.5 h at 585 °C (see Fig. 9f) reveal an inhomogeneous spatial distribution of UF austenite grains and Mn-enriched particles, providing further indication that these Mn-enriched particles eventually trigger austenite formation; not one of these particles is observed after 8 h of annealing. The small Mn-enriched particles are undoubtedly nuclei for the  $\alpha'$ -martensite/ferrite-to-austenite phase transformation whereas the compositions of some of the larger particles match Thermo-Calc<sup>®</sup> predictions of austenite composition (22 wt% Mn). These results indicate that during annealing, the excess Mn from the supersaturated parent  $\alpha'$ -martensite (Mn is an austenite stabilizer) produces Mn-enriched austenite nuclei during the early stages of intercritical annealing and could be the cause of sluggish and heterogeneous austenite nucleation [36,71,72].

The local equilibrium between austenite and  $\alpha'$ -martensite/ferrite predominantly governs the mechanism of austenite reversion and thus growth of UFG austenite [73,74]. Time- and space-dependent DICTRA simulations of a moving austenite interface that use a LE model are largely consistent with compositional profiles near phase boundaries measured with STEM-EDS and APT. In Fig. 12e–f, the shape of the Mn and C profiles within the austenite are similar for a given time step and indicate co-partitioning (consistent with APT results such as those in Fig. 9c–d). Austenite nucleation becomes more complex when the decomposition of a face-centered cubic (FCC)  $Mn_{23}C_6$  carbide is involved, as was shown by thermodynamic-kinetic simulations by Kwiatkowski da Silva et al. [37]. Following nucleation, later stages of austenite reversion and growth occurring between 0.5 h and 8 h follow the LE model for the moving interface between ferrite/recovered  $\alpha'$ -martensite and austenite. The compositions of UFG austenite and recovered  $\alpha'$ -martensite observed in the STEM-EDS linescan of Fig. 14f near the edge-on boundary reach almost constant equilibrium levels approximately 6 nm away from the boundary. APT results in Fig. 13f show a similar equilibration profile

in the austenite, but still a slight gradient of Mn concentration, from 8 to 6 at.% Mn, is observed in the recovered  $\alpha'$ -martensite within 40 nm of the austenite boundary. These concentration profiles are also consistent with recent DICTRA results [37] and confirm that austenite growth after 8 h of annealing is controlled by local equilibrium. In summary, the sequence of reversion in a Fe-12Mn-3Al-0.05C (wt%) steel is the following: (i) formation of Mn- and C-enriched FCC nuclei from Mn-decorated dislocations and/or particles; (ii) co-partitioning of Mn and C and (iii) growth of austenite controlled by the LE mode. Characteristic features measured by STEM-EDS and APT reveal Mn-depleted zones extending approximately 15–150 nm from the austenite interface and the absence of Mn-decorated defects within approximately 100 nm of the austenite interface in the neighboring recovered  $\alpha'$ -martensite.

#### 4.2. Reverted austenite boundary composition and mobility

Another consistent observation from APT results is the identification of C-enriched segments along boundaries between austenite and ferrite/recovered  $\alpha'$ -martensite, even after 8 h of annealing. Such results are consistent with other research focused on austenite-martensite interfaces [36,67,75]. The diffusivity of C in ferrite is more than two orders of magnitude greater than that in austenite [76], plus C favors and stabilizes austenite during intercritical annealing [9]. Since C diffusion is also much faster than the diffusion of substitutional elements (Fe, Mn, and Al), the observation of carbon enrichment and chemical gradients is surprising, especially for longer annealing times. Although considered, it is unlikely that room temperature aging plays a strong role in chemical gradients near phase boundaries as the diffusion coefficient is approximately 8 orders of magnitude lower at RT than at 600 °C [77]. However, the possible development of thin C-enriched regions at phase boundaries during the 100 °C/s quench from the intercritical annealing temperature cannot be dismissed, especially in the case where austenite borders a lath-like martensite boundary (lath size and defect content influence local composition) [78].

In samples annealed for 0.5 h and 8 h, C-enriched interfaces are observed at one of three boundaries in triple-junctions (Figs. 9d, 11c and 13c). Notably, the C-enriched boundary segments are usually extremely flat as shown in Fig. 9a/d and Fig. 13d/g, which provides a stark contrast to the curved parts of the same boundaries that are not C-enriched. Therefore, it is possible that the C enrichment is associated with stationary (flat) interfaces, which may relate to a local KS orientation relationship between austenite and recovered  $\alpha'$ -martensite (Fig. 13e) or a prior martensite-martensite straight boundary (Fig. 13a–c) [79]. The C-enriched interface of the triple-junction in Fig. 13a–c follows the low-angle lath boundary, but with a small opening angle and is likely the stationary interface during austenite reversion. The other austenite-martensite interfaces of the triple-junction in Fig. 13a–c (without C enrichment) evolve at a much larger angle from the previous lath boundary and are expected to be mobile and thereby control the austenite growth process. Furthermore, the observations of C enrichment at only some interfaces may truly be due to a combination of factors such as interface mobility/local growth velocity (parts of a triple-junction may be less mobile due to the shape/morphology of the nucleus [80,81]) or local crystallography [49] since parent  $\alpha'$ -martensite lath interfaces provide excellent traps for carbon [69,70,72,73,78,80,82]. On the other hand, C may form a separate phase at the interface [80,81,83–85]. Future work could usefully include more detailed analysis of APT needles using transmission Kikuchi diffraction and STEM imaging (before the APT measurements) in addition to correlative APT crystallography to provide more insight into whether or not the local crystallography significantly affects diffusion near interfaces [54,86].

#### 4.3. Factors influencing the morphology and size of grains during martensite recovery, austenite reversion and martensite recrystallization

Although the annealed microstructure contains recovered  $\alpha'$ -martensite, the martensite is not fresh athermal  $\alpha'$ -martensite formed from cooling, but rather resembles a recovered form of the cold-rolled microstructure (see Fig. 3a/d vs. Fig. 3b/e, Fig. 4a vs. Figs. 4b and 5a vs. Fig. 5d). Also, the partitioning of Mn and C to form austenite lowers the  $\alpha'$ -martensite start temperature below RT and inhibits the formation of fresh athermal  $\alpha'$ -martensite [9,10]. In the Fe-12Mn-3Al-0.05 wt% steel,  $T_{\gamma\text{-max}}$  is 630 °C (see Fig. 1) and thus greater than the chosen intercritical annealing temperature (585 °C). Additionally, thermodynamic predictions tend to underestimate  $T_{\gamma\text{-max}}$ , as compared to experimental measurements of austenite fraction as a function of annealing temperature, due to the effects of dislocation density and thus solute mobility [35]. The recovered microstructure (cell structures seen in Fig. 10h) can also be considered an incomplete recrystallization of the cold-rolled  $\alpha'$ -martensite [79], which is consistent with recent work by others [30,87] even on the same nominal composition of steel [8,20].

The recovered  $\alpha'$ -martensite contains a lower dislocation density than the cold-rolled  $\alpha'$ -martensite and includes regions where austenite reversion and formation of UFG ferrite have taken place. Equiaxed UFG austenite typically neighbors equiaxed UFG ferrite at locations in the microstructure where there is a high degree of misorientation (prior austenite grain boundaries and along high-angle martensite packet and block boundaries [88]). The equiaxed UFG ferrite is characterized by a larger grain size than that of the equiaxed UFG austenite (see Fig. 5), which is consistent with work by others [19,89] and indicates the small amount of observed martensite recrystallization precedes or occurs faster than the austenite growth in this material. Although Mn diffusion poses solute drag effects [90], there is clearly interdependence during intercritical annealing between the driving forces of  $\alpha'$ -martensite recrystallization and the reversion to UFG austenite. Arlazarov et al. [91] proposed that variations in dislocation density and Mn content in the  $\alpha'$ -martensite of a hot-rolled medium-Mn steel were coupled to the presence of polygonal ferrite and can aid in  $\alpha'$ -martensite recrystallization.

A 50% cold-rolled sample was further cold-rolled to 65% and subjected to a heat treatment of 8 h at 585 °C, which produced 32% austenite as measured by XRD. The slightly greater thickness reduction did not significantly increase the austenite fraction above that of the 50% cold-rolled samples annealed for 8 h at 585 °C (29% measured by XRD and 35% measured by EBSD, as seen in Table 1). Further, such a small difference may be within the error of phase fraction measurements from peak intensity summation as texture inherently influences the accuracy [92]. Such results indicate that the differences between 50% and 65% cold-rolled reductions are insufficient to produce significant changes in the annealed microstructure regarding austenite fraction. Based on work by Tokizane et al. [89], cold-rolled reductions would need to be on the order of 85% to significantly affect the size, fraction and morphology of the UFG austenite and UFG ferrite, since cold-rolling leads to a more inhomogeneous distribution of dislocations and cell structures in the deformed martensite [89]. However, a high density of carbide particles on grain boundaries can pin them and inhibit the recrystallization of martensite when governed by the bulge nucleation and growth mechanism [93]. It is also likely that cold-rolled reductions on the order of 85% would increase the austenite reversion kinetics by producing more equiaxed austenite instead of lamellar austenite without affecting the equilibrium fraction of austenite, even at lower annealing temperatures [89]. Thus, further manipulation of the recovered and elongated

microstructure for the Fe-12Mn-3Al-0.05C wt% steel would also require an increase in intercritical annealing time and temperature [8,19].

TEM and 2D EBSD results reveal UF equiaxed and rod-like austenite grains respectively near prior austenite grain boundaries and near parent  $\alpha'$ -martensite packet boundaries (see Fig. 7). Equiaxed UFG ferrite forms next to UFG equiaxed austenite, indicating an interrelation between recrystallization of  $\alpha'$ -martensite to form ferrite and reversion to austenite. EBSD results show that martensite-martensite (lath-lath) interfaces are low-angle, while ferrite and recovered  $\alpha'$ -martensite can be either low-angle or high-angle in character. Nearly all dissimilar phase boundaries (austenite-ferrite or austenite-recovered martensite) are high-angle. These misorientation observations indicate that the formation of UFG ferrite may not always be a true recrystallization phenomenon (nucleation and growth that produces mostly high-angle boundaries), but rather a recovery-based recrystallization (also referred to as recrystallization in situ). Moreover, the following parameters are decisive in achieving martensite recrystallization when in indirect competition with austenite reversion: dislocation density, inhomogeneity of dislocation density, intercritical annealing temperature, low carbon content (no Zener pinning of boundaries by cementite) and Mn content in martensite (grain boundary mobility) [49,89,93].

In addition to confirming the presence of recovered  $\alpha'$ -martensite, equiaxed UFG ferrite and equiaxed UFG austenite (see Figs. 3, Figs. 6, 7) and 3D EBSD results reveal some plate-like austenite grains (similar to those in a hot-rolled microstructure [79,88]) as well as equiaxed grains of similar orientation that are strung together like a necklace (see Fig. 8c–d). Martensite-martensite lath boundaries from the parent microstructure contain austenite grains that are more elongated and/or plate-like. Due to the absence of recrystallized UFG ferrite in these regions and the known presence of carbides near low-angle boundaries, the elongated austenite grains likely develop later in the reversion process.

Ultimately, tuning the mechanisms that control a resulting microstructure can have a pronounced effect on many categories of mechanical properties. Quantitatively characterizing multiple grain sizes and morphologies, as well as the compositional evolution of ultrafine-grained microstructural constituents requires a multi-scale approach. The present work focused on designing a multi-phase material with a suitable UFG austenite composition with a RT SFE such that strain-induced TWIP and TRIP effects are active during deformation, which was successful. Mechanical testing, analysis of deformation mechanisms and implementation of a realistic microstructure-based crystal-plasticity finite-element model (informed by dark-field TEM identification of deformation mechanisms and 3D EBSD measurements) are ongoing, but lie outside the scope of this paper.

## 5. Summary and conclusions

- A medium-Mn steel (Fe-12Mn-3Al-0.05C wt%) was designed using Thermo-Calc<sup>®</sup> simulations to balance the fraction and stacking fault energy of reverted austenite. Intercritical annealing for 0.5, 8 and 48 h was carried out at 585 °C to investigate the microstructural evolution. An increase in annealing time from 0.5 h to 48 h increases the amount of ultrafine-grained reverted austenite from 3 to 40 vol %.
- Quantitative compositional measurements with STEM-EDS and APT on samples of Fe-12Mn-3Al-0.05C (wt%) steel show some variations in Mn and C composition throughout austenite grains after 0.5 h of intercritical annealing at 585 °C. The mechanism of austenite reversion begins with formation of Mn- and C-

enriched face-centered-cubic nuclei (aided by Mn-enriched defects and/or particles), followed by Mn and C co-partitioning, and ends with growth of austenite controlled by the local equilibrium mode. In the early stages of austenite growth, the neighboring recovered  $\alpha'$ -martensite exhibits Mn-depleted zones that extend for 15–150 nm from the austenite interface and an absence of Mn-decorated defects within approximately 100 nm of the austenite. After 8 h of annealing at 585 °C, the phases are rather homogenous and the experimentally measured compositions are consistent with equilibrium Thermo-Calc<sup>®</sup> simulations: Fe-20.8Mn-2.1Al-0.11C wt% for austenite and Fe-4.9Mn-3.7Al-0.001C wt% for ferrite.

- Samples annealed for 0.5 h and 8 h contain flat segments of austenite-ferrite/recovered  $\alpha'$ -martensite boundaries that are C-enriched (up to 3 at.%) and appear less mobile. In addition to Mn depletion zones, triple-junctions and local orientation relationships play decisive roles in phase boundary mobility during austenite reversion.
- After intercritical annealing of the cold-rolled steel for 8 h at 585 °C, 3D EBSD and TEM reveal equiaxed UFG austenite, rod-like UFG austenite, plate-like UFG austenite, equiaxed UFG ferrite and recovered parent  $\alpha'$ -martensite. The parent microstructure does not completely recrystallize and still contains characteristics of the cold-rolled microstructure. Equiaxed UF austenite grains almost always nucleate near equiaxed UF ferrite grains. The equiaxed grains develop in regions of the microstructure with greater misorientation and/or dislocation densities, such as high-angle packet and block boundaries of the parent  $\alpha'$ -martensite and/or prior austenite triple-point grain boundaries. Rod-like and plate-like austenite grains form between low-angle laths/sub-blocks of the parent martensitic microstructure and likely develop later in the reversion process.

## Acknowledgements

This work was funded by the United States National Science Foundation (NSF) under grants NSF DMR 1309258 and NSF EPS 1004083. The Max-Planck-Institute für Eisenforschung in Düsseldorf, Germany and Thermo Scientific in Hillsboro, OR also provided resources necessary to complete this research. The authors are grateful to U. Tezins and A. Sturm for their technical support of the atom probe tomography and focused ion beam facilities at the Max-Planck-Institut für Eisenforschung. A.K.S. is grateful to the Brazilian National Research Council (Conselho Nacional de Pesquisas, CNPQ) for the Ph.D. scholarship through the “Science without Borders” Project (203077/2014-8).

## Appendix A. Supplementary data

Supplementary data to this article can be found online at <https://doi.org/10.1016/j.actamat.2019.01.003>.

## References

- [1] D.K. Matlock, J.G. Speer, Processing opportunities for new advanced high-strength sheet steels, *Mater. Manuf. Process.* 25 (2010) 1–3, <https://doi.org/10.1080/10426910903158272>, 7–13.
- [2] D.K. Matlock, J.G. Speer, Third generation of AHSS: microstructure design concepts, in: A. Haldar, S. Suwas, D. Bhattacharjee (Eds.), *Microstruct. Texture Steels*, Springer, London, 2009, pp. 185–205, [https://doi.org/10.1007/978-1-84882-454-6\\_11](https://doi.org/10.1007/978-1-84882-454-6_11).
- [3] D.T. Pierce, J.A. Jiménez, J. Bentley, D. Raabe, J.E. Wittig, The influence of stacking fault energy on the microstructural and strain-hardening evolution of Fe-Mn-Al-Si steels during tensile deformation, *Acta Mater.* 100 (2015) 178–190, <https://doi.org/10.1016/j.actamat.2015.08.030>.
- [4] D.R. Steinmetz, T. Jäpel, B. Wietbrock, P. Eisenlohr, I. Gutierrez-Urrutia, A. Saeed-Akbari, T. Hickel, F. Roters, D. Raabe, Revealing the strain-hardening behavior of twinning-induced plasticity steels: theory, simulations,

- experiments, *Acta Mater.* 61 (2013) 494–510, <https://doi.org/10.1016/j.actamat.2012.09.064>.
- [5] I. Gutierrez-Urrutia, S. Zaefferer, D. Raabe, The effect of grain size and grain orientation on deformation twinning in a Fe-22wt.% Mn-0.6wt.% C TWIP steel, *Mater. Sci. Eng.* 527 (2010) 3552–3560, <https://doi.org/10.1016/j.msea.2010.02.041>.
  - [6] Y.-K. Lee, J. Han, Current opinion in medium manganese steel, *Mater. Sci. Technol.* 31 (2015) 843–856, <https://doi.org/10.1179/1743284714Y.0000000722>.
  - [7] F. Yang, H. Luo, C. Hu, E. Pu, H. Dong, Effects of intercritical annealing process on microstructures and tensile properties of cold-rolled 7Mn steel, *Mater. Sci. Eng.* 685 (2017) 115–122, <https://doi.org/10.1016/j.msea.2016.12.119>.
  - [8] Y. Ma, W. Song, S. Zhou, A. Schwedt, W. Bleck, Influence of intercritical annealing temperature on microstructure and mechanical properties of a cold-rolled medium-Mn steel, *Metals* 8 (2018) 357, <https://doi.org/10.3390/met8050357>.
  - [9] S. Lee, B.C. De Cooman, On the selection of the optimal intercritical annealing temperature for medium Mn TRIP steel, *Metall. Mater. Trans.* 44 (2013) 5018–5024, <https://doi.org/10.1007/s11661-013-1860-2>.
  - [10] S. Lee, B.C. De Cooman, Annealing temperature dependence of the tensile behavior of 10 pct Mn multi-phase TWIP-TRIP steel, *Metall. Mater. Trans.* 45 (2014) 6039–6052, <https://doi.org/10.1007/s11661-014-2540-6>.
  - [11] S. Lee, S.J. Lee, S. Santhosh Kumar, K. Lee, B.C.D. Cooman, Localized deformation in multiphase, ultra-fine-grained 6 Pct Mn transformation-induced plasticity steel, *Metall. Mater. Trans.* 42 (2011) 3638–3651, <https://doi.org/10.1007/s11661-011-0636-9>.
  - [12] S. Lee, K. Lee, B.C. de Cooman, Observation of the TWIP + TRIP plasticity-enhancement mechanism in Al-added 6 Wt pct medium Mn steel, *Metall. Mater. Trans.* (2015) 1–8, <https://doi.org/10.1007/s11661-015-2854-z>.
  - [13] S. Lee, W. Woo, B.C. de Cooman, Analysis of the tensile behavior of 12 pct Mn multi-phase ( $\alpha + \gamma$ ) TWIP + TRIP steel by neutron diffraction, *Metall. Mater. Trans.* 47 (2016) 2125–2140, <https://doi.org/10.1007/s11661-016-3407-9>.
  - [14] C. Wang, W. Cao, J. Shi, C. Huang, H. Dong, Deformation microstructures and strengthening mechanisms of an ultrafine grained duplex medium-Mn steel, *Mater. Sci. Eng.* 562 (2013) 89–95, <https://doi.org/10.1016/j.msea.2012.11.044>.
  - [15] R. Zhang, W.Q. Cao, Z.J. Peng, J. Shi, H. Dong, C.X. Huang, Intercritical rolling induced ultra fine microstructure and excellent mechanical properties of the medium-Mn steel, *Mater. Sci. Eng.* 583 (2013) 84–88, <https://doi.org/10.1016/j.msea.2013.06.067>.
  - [16] M.C. McGrath, D.C. Van Aken, N.I. Medvedeva, J.E. Medvedeva, Work hardening behavior in steel with multiple TRIP mechanisms, *Metall. Mater. Trans.* 44 (2013) 4634–4643, <https://doi.org/10.1007/s11661-013-1820-x>.
  - [17] S.J. Lee, J. Kim, S.N. Kane, B.C. De Cooman, On the origin of dynamic strain aging in twinning-induced plasticity steels, *Acta Mater.* 59 (2011) 6809–6819, <https://doi.org/10.1016/j.actamat.2011.07.040>.
  - [18] M. Callahan, O. Hubert, F. Hild, A. Perlande, J.H. Schmitt, Coincidence of strain-induced TRIP and propagative PLC bands in Medium Mn steels, *Mater. Sci. Eng.* 704 (2017) 391–400, <https://doi.org/10.1016/j.msea.2017.08.042>.
  - [19] Y. Zhang, L. Wang, K.O. Findley, J.G. Speer, Influence of temperature and grain size on austenite stability in medium manganese steels, *Metall. Mater. Trans.* 48 (2017) 2140–2149, <https://doi.org/10.1007/s11661-017-3995-z>.
  - [20] M. Haupt, A. Dutta, D. Ponge, S. Sandlöbes, M. Nellesen, G. Hirt, Influence of intercritical annealing on microstructure and mechanical properties of a medium manganese steel, *Procedia Eng* 207 (2017) 1803–1808, <https://doi.org/10.1016/j.proeng.2017.10.942>.
  - [21] M.M. Wang, C.C. Tasan, D. Ponge, D. Raabe, Spectral TRIP enables ductile 1.1 GPa martensite, *Acta Mater.* 111 (2016) 262–272, <https://doi.org/10.1016/j.actamat.2016.03.070>.
  - [22] Y. Ma, Medium-manganese steels processed by austenite-reverted-transformation annealing for automotive applications, *Mater. Sci. Technol.* 33 (2017) 1713–1727, <https://doi.org/10.1080/02670836.2017.1312208>.
  - [23] R.L. Miller, Ultrafine-grained microstructures and mechanical properties of alloy steels, *Metall. Trans.* 3 (1972) 905–912, <https://doi.org/10.1007/BF02647665>.
  - [24] J. Han, S.H. Kang, S.J. Lee, Y.K. Lee, Fabrication of bimodal-grained Al-free medium Mn steel by double intercritical annealing and its tensile properties, *J. Alloy. Comp.* 681 (2016) 580–588, <https://doi.org/10.1016/j.jallcom.2016.04.014>.
  - [25] B.C. De Cooman, P. Gibbs, S. Lee, D.K. Matlock, Transmission electron microscopy analysis of yielding in ultrafine-grained medium Mn transformation-induced plasticity steel, *Metall. Mater. Trans.* 44 (2013) 2563–2572, <https://doi.org/10.1007/s11661-013-1638-6>.
  - [26] P.J. Gibbs, B.C. De Cooman, D.W. Brown, B. Clausen, J.G. Schroth, M.J. Merwin, D.K. Matlock, Strain partitioning in ultra-fine grained medium-manganese transformation induced plasticity steel, *Mater. Sci. Eng.* 609 (2014) 323–333, <https://doi.org/10.1016/j.msea.2014.03.120>.
  - [27] M. Koyama, Z. Zhang, M. Wang, D. Ponge, D. Raabe, K. Tsuzuki, H. Noguchi, C.C. Tasan, Bone-like crack resistance in hierarchical metastable nanolaminate steels, *Science* 355 (2017) 1055–1057, <https://doi.org/10.1126/science.aal2766>.
  - [28] G. Gao, H. Zhang, X. Gui, P. Luo, Z. Tan, B. Bai, Enhanced ductility and toughness in an ultrahigh-strength Mn-Si-Cr-C steel: the great potential of ultrafine filmy retained austenite, *Acta Mater.* 76 (2014) 425–433, <https://doi.org/10.1016/j.actamat.2014.05.055>.
  - [29] B.B. He, M.X. Huang, Strong and ductile medium Mn steel without transformation-induced plasticity effect, *Mater. Res. Lett.* 6 (2018) 365–371, <https://doi.org/10.1080/21663831.2018.1461141>.
  - [30] H. Lee, M.C. Jo, S.S. Sohn, A. Zargaran, J.H. Ryu, N.J. Kim, S. Lee, Novel medium-Mn (austenite + martensite) duplex hot-rolled steel achieving 1.6 GPa strength with 20 % ductility by Mn-segregation-induced TRIP mechanism, *Acta Mater.* 147 (2018) 247–260, <https://doi.org/10.1016/j.actamat.2018.01.033>.
  - [31] H.W. Yen, S.W. Ooi, M. Eizadjou, A. Breen, C.Y. Huang, H.K.D.H. Bhadeshia, S.P. Ringer, Role of stress-assisted martensite in the design of strong ultrafine-grained duplex steels, *Acta Mater.* 82 (2015) 100–114, <https://doi.org/10.1016/j.actamat.2014.09.017>.
  - [32] D. Yan, C.C. Tasan, D. Raabe, High resolution in situ mapping of microstrain and microstructure evolution reveals damage resistance criteria in dual phase steels, *Acta Mater.* 96 (2015) 399–409, <https://doi.org/10.1016/j.actamat.2015.05.038>.
  - [33] C.C. Tasan, M. Diehl, D. Yan, C. Zambaldi, P. Shanthraj, F. Roters, D. Raabe, Integrated experimental-simulation analysis of stress and strain partitioning in multiphase alloys, *Acta Mater.* 81 (2014) 386–400, <https://doi.org/10.1016/j.actamat.2014.07.071>.
  - [34] J. Chen, M. Lv, S. Tang, Z. Liu, G. Wang, Correlation between mechanical properties and retained austenite characteristics in a low-carbon medium manganese alloyed steel plate, *Mater. Char.* 106 (2015) 108–111, <https://doi.org/10.1016/j.matchar.2015.05.026>.
  - [35] E. De Moor, S. Kang, J.G. Speer, D.K. Matlock, Manganese diffusion in third generation advanced high strength steels, in: *Proc. Int. Conf. Mining, Mater. Metall. Eng.* 2014, pp. 1–7, in: [https://avestia.com/MMME2014\\_Proceedings/papers/Keynote\\_DeMoor.pdf](https://avestia.com/MMME2014_Proceedings/papers/Keynote_DeMoor.pdf).
  - [36] H. Luo, J. Shi, C. Wang, W. Cao, X. Sun, H. Dong, Experimental and numerical analysis on formation of stable austenite during the intercritical annealing of 5Mn steel, *Acta Mater.* 59 (2011) 4002–4014, <https://doi.org/10.1016/j.actamat.2011.03.025>.
  - [37] A. Kwiatkowski da Silva, G. Inden, A. Kumar, D. Ponge, B. Gault, D. Raabe, Competition between formation of carbides and reversed austenite during tempering of a medium-manganese steel studied by thermodynamic-kinetic simulations and atom probe tomography, *Acta Mater.* 147 (2018) 165–175, <https://doi.org/10.1016/j.actamat.2018.01.022>.
  - [38] D.T. Pierce, J.A. Jimenez, J. Bentley, D. Raabe, C. Oskay, J.E. Wittig, The influence of manganese content on the stacking fault and austenite/epsilon-martensite interfacial energies in Fe-Mn-(Al-Si) steels investigated by experiment and theory, *Acta Mater.* 68 (2014) 238–253, <https://doi.org/10.1016/j.actamat.2014.01.001>.
  - [39] J.T. Benzing, W.A. Poling, D.T. Pierce, J. Bentley, K.O. Findley, D. Raabe, J.E. Wittig, Effects of strain rate on mechanical properties and deformation behavior of an austenitic Fe-25Mn-3Al-3Si TWIP-TRIP steel, *Mater. Sci. Eng.* 711 (2018) 78–92, <https://doi.org/10.1016/j.msea.2017.11.017>.
  - [40] J.T. Benzing, J.E. Wittig, T.M. Smith, M.J. Mills, J.R. Johnson, G.S. Daehn, J. Bentley, D. Raabe, C. Ophus, Fe-25Mn-3Al-3Si TWIP-TRIP steel deformed at high strain-rates, *Microsc. Microanal.* 21 (Suppl 3) (2015) 1745–1746, <https://doi.org/10.1017/S1431927615009502>.
  - [41] J.T. Benzing, J. Bentley, W. Poling, K. Findley, D.T. Pierce, J.M. Sosa, H.L. Fraser, D. Raabe, J.E. Wittig, Microstructural characterization of a Fe-25Mn-3Al-3Si TWIP-TRIP steel, *Microsc. Microanal.* 22 (Suppl 3) (1962–1963), <https://doi.org/10.1017/S1431927616010655>, 2016.
  - [42] J.E. Jin, Y.K. Lee, Effects of Al on microstructure and tensile properties of C-bearing high Mn TWIP steel, *Acta Mater.* 60 (2012) 1680–1688, <https://doi.org/10.1016/j.actamat.2011.12.004>.
  - [43] Y.-K. Lee, S.-J. Lee, J. Han, Critical assessment: stacking fault energies of austenitic steels, *Mater. Sci. Technol.* (2016), <https://doi.org/10.1080/02670836.2015.1114252>, 160120043734007.
  - [44] Y.-K. Lee, C. Choi, Driving force for  $\gamma \rightarrow \epsilon$  martensitic transformation and stacking fault energy of  $\gamma$  in Fe-Mn binary system, *Metall. Mater. Trans.* 31 (2000) 355–360, <https://doi.org/10.1007/s11661-000-0271-3>.
  - [45] S.J. Lee, J. Han, C.Y. Lee, I.J. Park, Y.K. Lee, Elastic strain energy induced by epsilon martensitic transformation and its contribution to the stacking-fault energy of austenite in Fe-15Mn-xC alloys, *J. Alloy. Comp.* 617 (2014) 588–596, <https://doi.org/10.1016/j.jallcom.2014.08.054>.
  - [46] S. Morito, X. Huang, T. Furuhashi, T. Maki, N. Hansen, The morphology and crystallography of lath martensite in alloy steels, *Acta Mater.* 54 (2006) 5323–5331, <https://doi.org/10.1016/j.actamat.2006.07.009>.
  - [47] H. Kitahara, R. Ueji, N. Tsuji, Y. Minamino, Crystallographic features of lath martensite in low-carbon steel, *Acta Mater.* 54 (2006) 1279–1288, <https://doi.org/10.1016/j.actamat.2005.11.001>.
  - [48] L. Morsdorf, O. Jeannin, D. Barbier, M. Mitsuhashi, D. Raabe, C.C. Tasan, Multiple mechanisms of lath martensite plasticity, *Acta Mater.* 121 (2016) 202–214, <https://doi.org/10.1016/j.actamat.2016.09.006>.
  - [49] X. Zhang, G. Miyamoto, Y. Toji, S. Nambu, T. Koseki, T. Furuhashi, Orientation of austenite reverted from martensite in Fe-2Mn-1.5Si-0.3C alloy, *Acta Mater.* 144 (2018) 601–612, <https://doi.org/10.1016/j.actamat.2017.11.003>.
  - [50] C.S. Barrett, T.B. Massalski, *Structure of Metals, Third*, McGraw-Hill, 1966.
  - [51] S. Morito, Y. Adachi, T. Ohba, Morphology and crystallography of sub-blocks in ultra-low carbon lath martensite steel, *Mater. Trans.* 50 (2009) 1919–1923, <https://doi.org/10.2320/matertrans.MRA2008409>.
  - [52] M.P. Moody, B. Gault, L.T. Stephenson, D. Haley, S.P. Ringer, Qualification of the tomographic reconstruction in atom probe by advanced spatial

- distribution map techniques, *Ultramicroscopy* 109 (2009) 815–824, <https://doi.org/10.1016/j.ultramic.2009.03.016>.
- [53] L. Morsdorf, B. Gault, D. Ponge, C. Tasan, D. Raabe, Improved atom probe methodology for studying carbon redistribution in low-carbon high-mn lath martensitic steels, *Microsc. Microanal.* 23 (Suppl 1) (2017) 706–707, <https://doi.org/10.1017/S1431927617004196>.
- [54] A.J. Breen, K. Babinsky, A.C. Day, K. Eder, C.J. Oakman, P.W. Trimby, S. Primig, J.M. Cairney, S.P. Ringer, Correlating atom probe crystallographic measurements with transmission Kikuchi diffraction data, *Microsc. Microanal.* 23 (2017) 279–290, <https://doi.org/10.1017/S1431927616012605>.
- [55] J.T. Benzing, J. Bentley, J.R. McBride, D. Ponge, J. Han, D. Raabe, J.E. Wittig, Characterization of partitioning in a medium-Mn third-generation AHSS, *Microsc. Microanal.* 23 (Suppl 1) (2017) 402–403, <https://doi.org/10.1017/S1431927617002690>.
- [56] O.C. Hellman, J.A. Vandenbroucke, J. Rüsing, D. Isheim, D.N. Seidman, Analysis of three-dimensional atom-probe data by the proximity histogram, *Microsc. Microanal.* 6 (2000) 437–444, doi:10.1017/S1431927600000635.
- [57] A. Borgenstam, L. Höglund, J. Ågren, A. Engström, DICTRA, a tool for simulation of diffusional transformations in alloys, *J. Phase Equil.* 21 (2000) 269, doi:10.1361/105497100770340057.
- [58] A. Schneider, G. Inden, Simulation of the kinetics of precipitation reactions in ferritic steels, *Acta Mater.* 53 (2005) 519–531, <https://doi.org/10.1016/j.actamat.2004.10.008>.
- [59] G. Inden, P. Neumann, Simulation of diffusion controlled phase transformations in steels, *Steel Res. Int.* 67 (1996) 401–407, <https://doi.org/10.1002/srin.199605510>.
- [60] M.K. Miller, A. Cerezo, M.G. Hetherington, G.D.W. Smith, *Atom Probe Field-Ion Microscopy*, Oxford University Press, Oxford, 1996.
- [61] M.K. Miller, *Atom Probe Tomography*, first ed., Springer US, 2000 <https://doi.org/10.1007/978-1-4615-4281-0>.
- [62] B. Gault, M.P. Moody, J.M. Cairney, S.P. Ringer, *Atom Probe Microscopy*, first ed., Springer-Verlag, New York, 2012 <https://doi.org/10.1007/978-1-4614-3436-8>.
- [63] O. Dmitrieva, P. Choi, S.S.A. Gerstl, D. Ponge, D. Raabe, Pulsed-laser atom probe studies of a precipitation hardened maraging TRIP steel, *Ultramicroscopy* 111 (2011) 623–627, <https://doi.org/10.1016/j.ultramic.2010.12.007>.
- [64] J.J. Hren, J.I. Goldstein, D. Joy, N.J. Zaluzec, in: *Introduction to Analytical Electron Microscopy*, Plenum Press, New York, NY, 1979, pp. 121–167.
- [65] P.J. Goodhew, J. Humphreys, R. Beanland, *Electron Microscopy and Analysis*, Third, Taylor & Francis, London, 2001.
- [66] D.B. Williams, C. Barry Carter, *Transmission Electron Microscopy: A Textbook for Materials Science*, Springer US, 2009, <https://doi.org/10.1007/978-0-387-76501-3>.
- [67] E.J. Seo, L. Cho, B.C. De Cooman, Kinetics of the partitioning of carbon and substitutional alloying elements during quenching and partitioning (Q&P) processing of medium Mn steel, *Acta Mater.* 107 (2016) 354–365, <https://doi.org/10.1016/j.actamat.2016.01.059>.
- [68] A. Kwiatkowski da Silva, D. Ponge, Z. Peng, G. Inden, Y. Lu, A. Breen, B. Gault, D. Raabe, Phase nucleation through confined spinodal fluctuations at crystal defects evidenced in Fe-Mn alloys, *Nat. Commun.* 9 (2018) 1137, <https://doi.org/10.1038/s41467-018-03591-4>.
- [69] F.R. Beckitt, B.R. Clark, Shape and mechanism of formation of M23C6 carbide in austenite, *Acta Metall.* 15 (1967) 113–129, [https://doi.org/10.1016/0001-6160\(67\)90159-9](https://doi.org/10.1016/0001-6160(67)90159-9).
- [70] M. Belde, H. Springer, G. Inden, D. Raabe, Multiphase microstructures via confined precipitation and dissolution of vessel phases: example of austenite in martensitic steel, *Acta Mater.* 86 (2015) 1–14, <https://doi.org/10.1016/j.actamat.2014.11.025>.
- [71] S. Lee, B.C. De Cooman, Influence of carbide precipitation and dissolution on the microstructure of ultra-fine-grained intercritically annealed medium manganese steel, *Metall. Mater. Trans.* 47 (2016) 3263–3270, <https://doi.org/10.1007/s11661-016-3507-6>.
- [72] L. Yuan, D. Ponge, J. Wittig, P. Choi, J.A. Jiménez, D. Raabe, Nanoscale austenite reversion through partitioning, segregation and kinetic freezing: example of a ductile 2 GPa Fe-Cr-C steel, *Acta Mater.* 60 (2012) 2790–2804, <https://doi.org/10.1016/j.actamat.2012.01.045>.
- [73] F. Danoix, X. Sauvage, D. Huin, L. Germain, M. Gouné, A direct evidence of solute interactions with a moving ferrite/austenite interface in a model Fe-C-Mn alloy, *Scripta Mater.* 121 (2016) 61–65, <https://doi.org/10.1016/j.scriptamat.2016.04.038>.
- [74] H. Kamoutsi, E. Gioti, G.N. Haidemenopoulos, Z. Cai, H. Ding, Kinetics of solute partitioning during intercritical annealing of a medium-Mn steel, *Metall. Mater. Trans.* 46 (2015) 4841–4846, <https://doi.org/10.1007/s11661-015-3118-7>.
- [75] F. Huyan, J.Y. Yan, L. Höglund, J. Ågren, A. Borgenstam, Simulation of the growth of austenite from as-quenched martensite in medium Mn steels, *Metall. Mater. Trans.* 49 (2018) 1053–1060, <https://doi.org/10.1007/s11661-018-4497-3>.
- [76] T. Akbay, C. Atkinson, The influence of diffusion of carbon in ferrite as well as in austenite on a model of re-austenitization from ferrite/cementite mixtures in Fe-C steels, *J. Mater. Sci.* 31 (1996) 2221–2226, <https://doi.org/10.1007/BF01152931>.
- [77] C.A. Wert, Diffusion coefficient of C in  $\alpha$ -iron, *Phys. Rev.* 79 (1950) 601–605, <https://doi.org/10.1103/PhysRev.79.601>.
- [78] L. Morsdorf, C.C. Tasan, D. Ponge, D. Raabe, 3D structural and atomic-scale analysis of lath martensite: effect of the transformation sequence, *Acta Mater.* 95 (2015) 366–377, <https://doi.org/10.1016/j.actamat.2015.05.023>.
- [79] J. Chen, M. yang Lv, Z. yu Liu, G. dong Wang, Combination of ductility and toughness by the design of fine ferrite/tempered martensite-austenite microstructure in a low carbon medium manganese alloyed steel plate, *Mater. Sci. Eng.* 648 (2015) 51–56, <https://doi.org/10.1016/j.msea.2015.09.032>.
- [80] D. Raabe, S. Sandlöbes, J. Millán, D. Ponge, H. Assadi, M. Herbig, P.P. Choi, Segregation engineering enables nanoscale martensite to austenite phase transformation at grain boundaries: a pathway to ductile martensite, *Acta Mater.* 61 (2013) 6132–6152, <https://doi.org/10.1016/j.actamat.2013.06.055>.
- [81] O. Dmitrieva, D. Ponge, G. Inden, J. Millán, P. Choi, J. Sietsma, D. Raabe, Chemical gradients across phase boundaries between martensite and austenite in steel studied by atom probe tomography and simulation, *Acta Mater.* 59 (2011) 364–374, <https://doi.org/10.1016/j.actamat.2010.09.042>.
- [82] D. Raabe, M. Herbig, S. Sandlöbes, Y. Li, D. Tytko, M. Kuzmina, D. Ponge, P.P. Choi, Grain boundary segregation engineering in metallic alloys: a pathway to the design of interfaces, *Curr. Opin. Solid State Mater. Sci.* 18 (2014) 253–261, <https://doi.org/10.1016/j.cossms.2014.06.002>.
- [83] M. Kuzmina, M. Herbig, D. Ponge, S. Sandlöbes, D. Raabe, Linear complexions: confined chemical and structural states at dislocations, *Science* (80-. ) 349 (2015) 1080–1083, <https://doi.org/10.1126/science.aab2633>.
- [84] A. Kwiatkowski da Silva, G. Leyson, M. Kuzmina, D. Ponge, M. Herbig, S. Sandlöbes, B. Gault, J. Neugebauer, D. Raabe, Confined chemical and structural states at dislocations in Fe-9wt%Mn steels: a correlative TEM-atom probe study combined with multiscale modelling, *Acta Mater.* 124 (2017) 305–315, <https://doi.org/10.1016/j.actamat.2016.11.013>.
- [85] X. Zhang, T. Hicckel, J. Rogal, S. Fahler, R. Drautz, J. Neugebauer, Structural transformations among austenite, ferrite and cementite in Fe-C alloys: a unified theory based on ab initio simulations, *Acta Mater.* 99 (2015) 281–289, <https://doi.org/10.1016/j.actamat.2015.07.075>.
- [86] Y. Toji, H. Matsuda, M. Herbig, P.P. Choi, D. Raabe, Atomic-scale analysis of carbon partitioning between martensite and austenite by atom probe tomography and correlative transmission electron microscopy, *Acta Mater.* 65 (2014) 215–228, <https://doi.org/10.1016/j.actamat.2013.10.064>.
- [87] S.S. Sohn, H. Song, B.C. Suh, J.H. Kwak, B.J. Lee, N.J. Kim, S. Lee, Novel ultra-high-strength (ferrite + austenite) duplex lightweight steels achieved by fine dislocation substructures (Taylor lattices), grain refinement, and partial recrystallization, *Acta Mater.* 96 (2015) 301–310, <https://doi.org/10.1016/j.actamat.2015.06.024>.
- [88] J. Han, A.K. da Silva, D. Ponge, D. Raabe, S.M. Lee, Y.K. Lee, S.I. Lee, B. Hwang, The effects of prior austenite grain boundaries and microstructural morphology on the impact toughness of intercritically annealed medium Mn steel, *Acta Mater.* 122 (2017) 199–206, <https://doi.org/10.1016/j.actamat.2016.09.048>.
- [89] M. Tokizane, N. Matsumura, K. Tsuzaki, T. Maki, I. Tamura, Recrystallization and formation of austenite in deformed lath martensitic structure of low carbon steels, *Metall. Trans. A.* 13 (1982) 1379–1388, <https://doi.org/10.1007/BF02642875>.
- [90] Y. Li, W. Li, N. Min, W. Liu, X. Jin, Effects of hot/cold deformation on the microstructures and mechanical properties of ultra-low carbon medium manganese quenching-partitioning-tempering steels, *Acta Mater.* 139 (2017) 96–108, <https://doi.org/10.1016/j.actamat.2017.08.003>.
- [91] A. Arlazarov, M. Gouné, O. Bouaziz, A. Hazotte, G. Petitgand, P. Barges, Evolution of microstructure and mechanical properties of medium Mn steels during double annealing, *Mater. Sci. Eng.* 542 (2012) 31–39, <https://doi.org/10.1016/j.msea.2012.02.024>.
- [92] A. Creuziger, C.A. Calhoun, W.A. Poling, T. Gnäupel-Herold, Assessment of bias errors caused by texture and sampling methods in diffraction-based steel phase measurements, *J. Appl. Crystallogr.* 51 (2018) 720–731, <https://doi.org/10.1107/S160057671800420X>.
- [93] T. Tsuchiyama, Y. Miyamoto, S. Takaki, Recrystallization of lath martensite with bulge nucleation and growth mechanism, *ISIJ Int.* 41 (2001) 1047–1052, <https://doi.org/10.2355/isijinternational.41.1047>.